

1 **PEA15 loss of function and defective cerebral development in the domestic cat**

2

3 Emily C. Graff<sup>1,4,5, †\*</sup>, J. Nicholas Cochran<sup>2, †</sup>, Christopher B. Kaelin<sup>2</sup>, Kenneth Day<sup>2</sup>, Heather L.  
4 Gray-Edwards<sup>3,4</sup>, Rie Watanabe<sup>1</sup>, Jey W. Koehler<sup>1,5</sup>, Rebecca A. Falgoust<sup>4</sup>, Jeremy W. Prokop<sup>2</sup>,  
5 Richard M. Myers<sup>2</sup>, Nancy R. Cox<sup>3,4</sup>, Gregory S. Barsh<sup>2</sup>, Douglas R. Martin<sup>3,4,5</sup>; 99 Lives  
6 Consortium<sup>‡</sup>

7

8 **Affiliations:**

9 <sup>1</sup>Department of Pathobiology, College of Veterinary Medicine, Auburn University, Auburn,  
10 Alabama, USA

11 <sup>2</sup>HudsonAlpha Institute for Biotechnology, Huntsville, AL, USA

12 <sup>3</sup>Department of Anatomy Physiology and Pharmacology, College of Veterinary Medicine,  
13 Auburn University, Auburn, Alabama, USA

14 <sup>4</sup>Scott-Ritchey Research Center, College of Veterinary Medicine, Auburn University, Auburn,  
15 Alabama, USA

16 <sup>5</sup>Center for Neuroscience Initiative, Auburn University, Auburn, AL, USA

17

18 \*Corresponding author: Correspondence should be addressed to Emily Graff

19 ([ecg0001@auburn.edu](mailto:ecg0001@auburn.edu)), Doug Martin ([martidr@auburn.edu](mailto:martidr@auburn.edu)), or Greg Barsh

20 ([gbarsh@hudsonalpha.org](mailto:gbarsh@hudsonalpha.org)).

21 <sup>†</sup>These authors contributed equally to this work.

22 <sup>‡</sup>See Acknowledgements for list of members

23

24

25

26 **Abstract**

27 Cerebral cortical size and organization are critical features of neurodevelopment and human  
28 evolution, for which genetic investigation in model organisms can provide insight into  
29 developmental mechanisms and the causes of cerebral malformations. However, some  
30 abnormalities in cerebral cortical proliferation and folding are challenging to study in laboratory  
31 mice due to the absence of gyri and sulci in rodents. We report an autosomal recessive allele in  
32 domestic cats associated with impaired cerebral cortical expansion and folding, giving rise to a  
33 smooth, lissencephalic brain, and that appears to be caused by homozygosity for a frameshift in  
34 *PEA15* (phosphoprotein expressed in astrocytes-15). Notably, previous studies of a *Pea15*  
35 targeted mutation in mice did not reveal structural brain abnormalities. Affected cats, however,  
36 present with a non-progressive hypermetric gait and tremors, develop dissociative behavioral  
37 defects and aggression with age, and exhibit profound malformation of the cerebrum, with a 45%  
38 average decrease in overall brain weight, and reduction or absence of the ectosylvian, sylvian  
39 and anterior cingulate gyrus. Histologically, the cerebral cortical layers are disorganized, there is  
40 substantial loss of white matter in tracts such as the corona radiata and internal capsule, but the  
41 cerebellum is relatively spared. RNA-seq and immunohistochemical analysis reveal astrocytosis.  
42 Fibroblasts cultured from affected cats exhibit increased TNF $\alpha$ -mediated apoptosis, and  
43 increased FGFb-induced proliferation, consistent with previous studies implicating PEA15 as an  
44 intracellular adapter protein, and suggesting an underlying pathophysiology in which increased  
45 death of neurons accompanied by increased proliferation of astrocytes gives rise to abnormal  
46 organization of neuronal layers and loss of white matter. Taken together, our work points to a new  
47 role for *PEA15* in development of a complex cerebral cortex that is only apparent in gyrencephalic  
48 species.

49

50 **Key Words:** cat; autosomal recessive; neurodevelopment; PEA15; lissencephaly; sulci; gyri

51 **Summary**

52 Gyrfication is the neurodevelopmental process in certain mammalian species during which the  
53 cerebral cortex expands and folds resulting in the classic wrinkled appearance of the brain.  
54 Abnormalities in this process underlie many congenital malformations of the brain. However,  
55 unlike many other human malformations, genetic insight into gyrfication is not possible in  
56 laboratory mice because rodents have a lissencephalic or smooth cerebral cortex. We identified  
57 a mutation in domestic cats that likely causes failure of the cerebral cortex to expand and fold  
58 properly, and discovered that the mutation impairs production of a protein, PEA15  
59 (phosphoprotein expressed in astrocytes-15), involved in intracellular signaling. Affected cats  
60 have profound abnormalities in brain development, with minimal changes in their superficial  
61 behavior and neurologic function. Additional studies of tissue and cultured cells from affected  
62 animals suggest a pathophysiologic mechanism in which increased death of neurons  
63 accompanied by increased cell division of astrocytes gives rise to abnormal organization of  
64 neuronal layers and loss of white matter. These results provide new insight into a developmental  
65 process that is unique to animals with gyrencephalic brains.

## 66 Introduction

67 Cerebral dysgenesis, or abnormal development of the telencephalon, encompasses a large  
68 number of malformations of cortical development including cortical dysplasia, microcephaly,  
69 heterotopia, schizencephaly, and polymicrogyria [1]. Clinical presentation of patients with cerebral  
70 dysgenesis can range from intellectual disability to severe epilepsy and neural tube defects [2].  
71 Mendelian causes of cerebral dysgenesis in humans includes loss of function mutations in  
72 *WDR62*, *NDE1*, *DYNC1H1*, *KIF5C*, *KIF2A*, and *TUBG1* and related genes [3]. The vast majority  
73 of genes that regulate advanced cerebral cortical development have been discovered via forward  
74 genetic approaches in humans.

75 Gyrification refers to the process by which the cerebral cortex expands and folds. Overall  
76 size and gyrification of the cerebral cortex varies significantly between species [4], and increased  
77 cortical mass, cortical gyrification, and complex lamination within the cerebral cortex are traits that  
78 are associated with cognitive ability [5, 6]. Appropriate *in vivo* models of gyrification are limited  
79 as most laboratory animals exhibit minimal gyrification, and rodents (the most commonly used  
80 laboratory models) are lissencephalic [4]. However, the few studies that do exist in gyrencephalic  
81 models provide important insights into mechanisms of gyrification [7, 8], and gyrification studies  
82 are being conducted in relevant gyrencephalic species such as cats, sheep, and dogs [4]. Cats  
83 have prominent gyrification and are commonly used as a model for numerous neurologic diseases  
84 [9, 10].

85 Here we report that a loss of function mutation in *PEA15* (FelCat9 Chr. F1, 66768323 GT  
86 -> G) is likely responsible for a form of cerebral dysgenesis in the domestic cat, characterized by  
87 microcephaly and polymicrogyria. Characterization of the pathophysiological and  
88 neurodevelopmental consequences of *PEA15* deficiency offers insight into its essential role in  
89 gyrification and cortical development.

90

## 91 Results

92 *Cerebral dysgenesis underlies an inherited neurodevelopmental abnormality in cats*

93 An autosomal recessive, neurodevelopmental abnormality spontaneously arose in a domestic cat  
94 research colony at Auburn University. The mutation originated during outbreeding of cats used  
95 to study two lysosomal storage diseases, in which mutations were segregating for GM2  
96 gangliosidosis variant AB (*GM2A*) [11], and mucopolysaccharidosis VI (*MPSVI*) [12]. The cerebral  
97 dysgenesis phenotype segregated independently from both of the known mutations in the colony  
98 (Table S1) and is clinically distinct from the lysosomal storage disease phenotypes, which lead to  
99 a progressive neurologic degeneration that is typically fatal prior to one year of age. Evaluation of  
100 123 cats from the two breeding colonies identified 25 cats that were phenotypically affected with  
101 cerebral dysgenesis (S1 Figure). Of these affected cats, six were heterozygous, and three were  
102 homozygous for the *MPSVI* mutant allele, while one was heterozygous and three were  
103 homozygous for the *GM2A* mutant allele. None of the cats with cerebral dysgenesis were doubly  
104 homozygous for *MPSVI* and *GM2A* mutant alleles, and expressivity of the cerebral dysgenesis  
105 phenotype was not affected by carrier status of either *MPSVI* or *GM2A*.

106 Animals with cerebral dysgenesis exhibit spastic tetraparesis and ataxia first apparent  
107 around 3–4 weeks of age as they begin to walk. As the animals grow, spasticity and ataxia partially  
108 resolve, stabilizing by 6–9 months of age. At approximately 1.5 years, affected cats develop  
109 sensory abnormalities and often become aggressive. Sensory abnormalities manifest as  
110 stargazing and fly-biting: staring into empty space, and attacking or biting with no stimulus  
111 present, respectively. Aggressive behaviors were often erratic, unpredictable and included  
112 unprovoked attacks on long-term cage mates and caretakers. Some affected animals had  
113 seizures, although abnormal baseline EEG tracings were not observed. There were no deviations  
114 from reference intervals in complete blood count, serum biochemistry or urinalysis of affected  
115 cats, indicating that apart from the severe neurologic changes there was no additional systemic  
116 disease. Cerebrospinal fluid in carriers and affected cats showed no abnormalities or evidence of  
117 central nervous system inflammation (Table S2). In addition, cerebrospinal fluid enzyme activity

118 for markers of inflammation and neuronal cell damage were not significantly different from  
119 unaffected age-matched cats (S2 Figure). Taken together, these findings suggest that affected  
120 adult cats had a stable, non-progressive neurologic disease.

121 At necropsy, affected juvenile and adult cats exhibited generalized microcephaly and  
122 polymicrogyria with focal lissencephaly and regional gyral variability (Figure 1A - 1C). The most  
123 severely affected areas (frontoparietal) often had a cobblestone appearance. The average brain  
124 weight of affected cats was 4.3 grams per kilogram of body weight, while for unaffected and carrier  
125 cats average brain weight was 7.8 grams per kilogram, indicating a 45% decrease in brain mass  
126 (Figure 1D). In contrast to the significant abnormalities in the cerebral cortex, the size and  
127 structure of the cerebellum was normal with no vermal or hemispheric hypoplasia, dysplasia or  
128 agenesis.

129 Brains from affected cats aged 1–8 months were evaluated histologically in comparison  
130 to aged-matched controls (Figure 1E). Overall, affected cats exhibited variable thinning of the  
131 cerebral cortex, especially in dorsal and lateral regions, and disorganization of cortical layers. In  
132 severely affected areas, cortical neurons were present in an undulating laminar band reminiscent  
133 of gyri, but sulci were largely absent and gyral folds were irregular in size, location, distribution,  
134 and orientation. White matter of the corona radiata and internal capsule was markedly decreased  
135 in volume, but the corpus callosum was generally spared. Basal nuclei appeared normally  
136 organized, as did olfactory tubercles, olfaction tracts and thalamus, although all areas were  
137 smaller than age-matched controls. Recapitulating the impressions garnered at necropsy, the  
138 cerebellum was normally organized with all layers including an age-appropriate external granule  
139 layer in cats younger than 3–4 months.

140 Magnetic resonance imaging (MRI) showed similar gyrification abnormalities as observed  
141 grossly in necropsy samples with flattening of the parietal and temporal lobes (Figure 2).  
142 Additionally, MRI suggested that decreased brain volume was due primarily to decreased white  
143 matter. The most dramatic changes noted on MRI were located at the perisylvian, ectosylvian and

144 cingulate gyri (Figure 2A – 2C), where there was serve attenuation of gyral formation and  
145 decreased white matter, particularly in the anterior region (Figure 2C).

146

147 *PEA15 loss of function as the most likely Mendelian cause of cerebral dysgenesis.*

148 To identify the underlying genetic cause of cerebral dysgenesis, we initially carried out whole  
149 genome sequencing (WGS) and RNA-seq-based genotyping of eight affected animals and six  
150 obligate carriers, applying zygosity-based filtering criteria under the model of complete  
151 penetrance of an autosomal recessive trait. We identified all variants that were homozygous in  
152 eight affected animals and heterozygous in the six obligate carriers, and observed a cluster of  
153 variants that was significantly enriched ( $p = 0.006$ , chi-square vs. random genome-wide  
154 distribution) in a 5 Mb region towards the end of chromosome F1 (Figure 3A).

155 To confirm and further fine-map the region, we carried out amplicon-based genotype-by-  
156 sequencing on an additional 91 cats (Figure 3, Table S1), using 26 variants across an ~70 Mb  
157 interval that contains the candidate region on chromosome F1, 4 additional variants that span the  
158 remainder of chromosome F1, and 20 variants from other chromosomes. All affected cats, but  
159 no unaffected cats, were homozygous for a 1.3 Mb haplotype on chromosome F1 (Figure 3B) in  
160 which the peak LOD score was 10.1 (Figure 3C, Table S3); all variants on chromosomes other  
161 than F1 exhibited LOD scores  $< 1.8$  (Table S3).

162 Within the 1.3 Mb critical region, there are 2289 variants, of which 337 are not present in  
163 the 99 Lives dataset (an allele frequency database for cats described elsewhere [13]), including  
164 4 in protein-coding sequence. Among all variants for which human orthology could be assigned,  
165 one, a single nucleotide deletion in *PEA15* (FelCat9 Chr. F1, 66768323 GT -> G), stood out as  
166 exhibiting the highest level of potential deleteriousness as assessed with combined annotation  
167 dependent depletion (CADD) (Figure 3D). The remaining 3 coding variants were either  
168 synonymous or not predicted to be damaging (Table 1), and lie in 2 genes that are not expressed

169 in brain (*ATP1A4*, 2 counts per million; *LY9*, 3 counts per million). By contrast, *PEA15* is highly  
170 expressed cat brain cortex by RNA-seq (401 counts per million) described further below.

171 In addition to considering single nucleotide and small indel variants, we surveyed the  
172 critical region for copy number and structural variants (Methods), and did not detect any changes  
173 consistent with the previously observed zygosity pattern. Furthermore, no assembly or coverage  
174 gaps were present in the 1.3 Mb candidate interval, and we found no evidence for structural  
175 variants based on discordant or clipped reads (Figure S3).

176 In cats and other species, including humans, *PEA15* encodes a 15 kDa protein of 130  
177 amino acids that is highly conserved across species (Figure S4). The nucleotide deletion in  
178 *PEA15* lies towards the beginning of the second exon, and predicts a frameshift and truncated  
179 protein that lacks a critical ERK2 interaction domain (Figure 4A). Expression levels of *PEA15* as  
180 assessed by RNA-seq (described below) from the cerebral cortex of adult cats reveal a reduction  
181 of 59% in homozygous affected animals, consistent with nonsense-mediated decay (NMD)  
182 (Figure 4B). In further support of NMD, in cats that are heterozygous for the 1.3 Mb critical region,  
183 we observed a significant allele bias in *PEA15* compared to other genes in the critical region  
184 (Figure 4C). We examined protein levels by Western blot with a polyclonal antibody against C-  
185 terminal amino acids 93-123 of Human *PEA15*; a 15 kDa band apparent in normal brain extracts  
186 was absent in brains from affected animals (Figure 4D).

187

188 *Neuropathology of cerebral dysgenesis.*

189 MAP2 immunohistochemically (IHC) stained sections (Figure 5A) were assessed along with Luxol  
190 fast blue (LFB) histochemical stained sections (Figure 5B) to evaluate changes in grey matter  
191 thickness and overall white matter area. Affected cats had variably decreased cortical grey matter  
192 thickness compared to age-matched controls (Figure 5A), and marked reduction of the white  
193 matter that comprises the corona radiata and internal capsule (Figure 5B). Consistent with MRI



194 evaluation, there was an overall decrease in white matter which resulted in decreased area of  
195 LFB staining (Figure 5C).

196 Cortical layering in affected cats was more disorganized and variable in layer thickness  
197 compared to unaffected cats. Visually distinct cell populations like large pyramidal neurons were  
198 present (Figure 6A). The molecular layer was more prominent in LFB and GFAP stained sections  
199 owing to increased astrocyte density (Figure 6B). In unaffected cats, there were linear axonal  
200 projections that were oriented perpendicularly to the cortical meningeal surface. In cats with  
201 cerebral dysgenesis, perpendicular axonal orientation was reduced, with a denser and more  
202 haphazard orientation of neuronal processes as compared to unaffected cats (Figure 6C).

203 We assessed the density of astrocytes, cells of oligodendrocytic origin, and microglia by  
204 histomorphometry after immunostaining sections for GFAP, Olig-2, and IBA-1, respectively. The  
205 only significant change in affected cats was an increase in staining density for GFAP, due to  
206 increased numbers of grey matter astrocytes (Figure 7A-E). There was no significant difference  
207 observed in Olig-2 staining (Figure 7F-J), however it should be noted that Olig-2 detects both  
208 oligodendrocytic precursor cells, which can differentiate into neurons, astrocytes, and  
209 oligodendrocytes, as well as mature myelinating oligodendrocytes. No difference was detected in  
210 microglial density or morphology (Figure 7K-O).

211

### 212 *RNA-seq analysis*

213 To better understand the pathophysiologic mechanisms underlying cerebral dysgenesis, we  
214 analyzed RNA-seq data from cerebral cortex of adult homozygous mutant (n=4), heterozygous  
215 (n=3), and non-mutant (n=3) cats. 61 genes exhibited significant (FDR <0.05) differential  
216 expression between homozygous mutant and non-mutant cats. Only 3 genes exhibited differential  
217 expression between heterozygous mutant and non-mutant cats. Given minimal differences by  
218 RNA-seq and that heterozygous mutant cats are unremarkable phenotypically, we also performed  
219 a comparison of all 6 unaffected cats vs. homozygous mutant cats, revealing 25 differentially

220 expressed (FDR <0.05) genes. The intersection of genes that were differentially expressed in  
221 both the all unaffected vs. homozygous mutant comparison and non-mutant vs. homozygous  
222 mutant comparison results in a list of 16 differentially expressed genes (Figure 8A; Supplemental  
223 Table 4), including 5 upregulated collagen genes (*COL6A5*, *COL4A5*, *COL3A1*, *COL1A1*, and  
224 *COL6A1*; Figure 8B).

225 These observations, together with the neuropathologic observations that suggested  
226 profound abnormalities in cerebral development and cellular organization, suggested that gene  
227 expression changes in cortex might be utilized to assess changes in cellular composition. To  
228 explore this further, we analyzed the RNA-seq data with cell type-specific deconvolution analysis  
229 [14], in which genes are organized and plotted according to their differential expression, the extent  
230 of enrichment in a specific cell type, and the nominal significance of that observation. As depicted  
231 in Figure 9, many transcripts enriched in oligodendrocyte precursor cells are overrepresented  
232 (Figure 9A), while many transcripts enriched in mature oligodendrocytes are underrepresented  
233 (Figure 9B). Transcripts for mature astrocytes (Figure 9C) and endothelial cells (Figure 9D) also  
234 exhibited a slight but significant enrichment, while no differences were observed for neurons or  
235 microglia (Figure 9E, 9F). Overall, these results are consistent with the histomorphometry data,  
236 and suggest a pathologic mechanism in which axonal disorganization, failure of gyrification, and  
237 microcephaly are secondary to expansion of astrocytes and reduction of myelin-associated cells.

238

#### 239 *Effects of PEA15 deficiency on apoptosis and cell proliferation in cats.*

240 Previous studies of *PEA15* in mice using a gene-targeted allele and a transgenic overexpression  
241 model demonstrated that it normally functions to suppress both TNF $\alpha$ -induced apoptosis [15] and  
242 cell proliferation during wound closure [16, 17]. We examined primary fibroblasts cultured from  
243 affected homozygous and non-mutant cats to investigate if those functions were conserved  
244 across species.

245           After treatment with TNF $\alpha$ , fibroblasts from affected animals exhibited reduced cell viability  
246 (Figure 9A) and increased caspase-8 activity (Figure 10B). Cell viability and caspase 8 activity  
247 did not change in the absence of TNF $\alpha$  treatment in fibroblasts from affected or unaffected  
248 animals. Exposure to FGFb for 72 hours yielded an ~ 2.5-fold increase in cell number in fibroblasts  
249 from unaffected animals, significantly elevated ( $p = 0.02$ ) to ~3.5-fold in fibroblasts from affected  
250 animals (Figure 10C). Taken together, these results confirm that the effects of *PEA15* on  
251 apoptosis and cell proliferation are similar in cats and mice, and illustrate the functional impact of  
252 the *PEA15* mutation in cats with cerebral dysgenesis.

253

## 254 **Discussion**

255 *PEA15* was originally described more than 25 years ago as a substrate for protein kinase C that  
256 is associated with microtubules and highly enriched in astrocytes [18]. Subsequent studies  
257 indicated that *PEA15* is expressed at low levels in almost all tissues [19] but exhibits increased  
258 expression in the brain, particularly during late gestation and the early postnatal period [20]. In  
259 mouse fibroblasts, *PEA15* was characterized as an adapter protein that regulates proliferation  
260 through cytoplasmic interaction with ERK1/2 [21-23], and receptor-mediated apoptosis through  
261 interaction with the Fas-associated death domain (FADD) [18]. Many studies on *PEA15* have  
262 focused on a potential role in insulin resistance due to its increased expression in fibroblasts,  
263 skeletal muscle, and adipose tissue during states of insulin resistance (reviewed elsewhere  
264 [24]). *Pea15* knockout mice exhibited normal brain size and morphology [15], but displayed mild  
265 spatial and temporal learning deficits attributed to the potential role of *PEA15* as a mediator of  
266 ERK-dependent spatial learning [25].

267           The *PEA15* frameshift mutation we identified in domestic cats is associated with a loss  
268 of steady state mRNA and immunodetectable protein, and fibroblasts homozygous for the  
269 mutation exhibit abnormalities in response to TNF $\alpha$  and FGFb that recapitulate what has been  
270 described previously in mice and mouse cells. In contrast to mutant mice, however, in which

271 there are no obvious abnormalities in brain development, *PEA15* deficiency in cats is associated  
272 with extensive abnormalities in development and organization of the cerebral cortex that lead to  
273 a 45% decrease in overall brain weight, defective gyrification, expansion of astrocytes, and a  
274 loss of mature oligodendrocytes and white matter. Complete genomic sequence over the critical  
275 interval within which the cerebral dysgenesis mutation must lie identified no other plausible  
276 candidate variants except the *PEA15* frameshift mutation, and we conclude that *PEA15*  
277 deficiency is the likely cause of the neuropathologic abnormalities. Unlike many other domestic  
278 animals, application of gene editing technology to domestic cats faces a number of barriers and  
279 challenges, so it is not possible at present to further explore the pathogenicity of *PEA15* by  
280 generating new alleles, as might typically take place in laboratory mice. Nonetheless, there is a  
281 preponderance of evidence supporting a causal role for *PEA15* in cerebral dysgenesis, and we  
282 suggest that failure to observe a similar phenotype in mice has a simple explanation: the rodent  
283 brain is normally lissencephalic, and thus does not depend on extensive neuronal proliferation,  
284 expansion, and gyrification as it does in cats, dogs, and primates.

285 We propose a neuropathologic mechanism for the abnormalities described here whereby  
286 *PEA15* normally serves to negatively regulate neuronal apoptosis and astrocyte proliferation  
287 (Figure 11, left), as has been demonstrated previously in mice. In the absence of *PEA15*,  
288 increased neuronal apoptosis and astrocyte proliferation leads to the production of excessive  
289 perineuronal nets, axonal disorganization and underdeveloped white matter tracts (Figure 11,  
290 right). Additional studies of *PEA15*-deficient cats should help determine at which phase of  
291 cortical development—neuroepithelial stem cell proliferation, neuronal stem cell migration, or  
292 synaptogenesis, apoptosis, and synaptic pruning—the postulated mechanisms are operative.  
293 We note, however, that the temporal pattern of *PEA15* expression, which peaks during late  
294 gestation and the early postnatal period, suggests a major role in the later stages of brain  
295 development, i.e. regulating neuronal apoptosis during synaptogenesis and synaptic pruning.

296           Although brain abnormalities in *PEA15*-deficient cats are striking, their gross appearance  
297 and behavior is not. Affected kittens were initially recognized due to a mild ataxia and were  
298 described by the husbandry staff as “shaky”; however, this gradually stabilized with age, and  
299 phenotype-based inference of disease status depends on an experienced clinician. Nonetheless,  
300 *PEA15* is under strong purifying selection—there is only a single amino acid substitution among  
301 mouse, cat, and human—and the gnomAD 2.1.1 [26] and TOPMed Bravo databases of human  
302 genome and exome data contains only 11 heterozygous loss-of-function variants (with none in  
303 the homozygous state) out of 198,527 non-overlapping individuals. Extrapolation suggests  
304 approximately five individuals on the planet with homozygous or compound heterozygous loss-  
305 of-function *PEA15* variants (assuming such a state would be consistent with life in humans), which  
306 may explain why it has not been previously recognized as a cause of human lissencephaly. In a  
307 recent summary of targeted sequencing studies for 17 genes in 811 patients with lissencephaly,  
308 a diagnostic rate of 81% was observed, in which > 99% of mutations were in *LIS1*, *DCX*, *TUBA1A*,  
309 or *DYNC1H1*, none of which are inherited in an autosomal recessive fashion.

310           In addition to identification of *PEA15* as a candidate gene for human lissencephaly, our  
311 work provides a new opportunity to investigate developmental mechanisms that underlie unique  
312 aspects of neurodevelopment in gyrencephalic species. Many of the processes disrupted by  
313 mutations in *LIS1*, *DCX*, *TUBA1A*, or *DYNC1H1* affect neuronal migration early in brain  
314 development, but, as noted above, the major role for *PEA15* in cortical development may occur  
315 later. As genomic tools for non-human animals continue to progress, careful clinical studies of  
316 companion and domestic animals are likely to lead to new insights into developmental and  
317 physiologic processes that are not present in conventional laboratory models.

318

## 319 **Materials and Methods:**

320 *Study subjects and ethics statement*

321 Animals included in this study are from the research colony at Auburn University College of  
322 Veterinary Medicine's Scott-Ritchey Research Center. Institutional Animal Care and Use  
323 Committee (IACUC) approval was obtained for all animal experiments. Animals evaluated in this  
324 study ranged in age from 1.2 months to 16 years and were evaluated in part based on videos that  
325 spanned a 20 year period. Based on breeding history, three adult cats within the colony were  
326 determined to be carriers. These cats along with three affected adults were also assessed by  
327 physical exam, including a complete neurological exam, serum biochemical analysis, complete  
328 blood count, MRI, and cerebrospinal fluid analysis. Cats were also evaluated for abnormalities  
329 associated with mutation in *GM2A* [11], and mucopolysaccharidosis VI (*MPSVI*) [12] which were  
330 independent of the phenotype observed here as described in the main text. Images of tissues  
331 depicted in Figures 1, 5, 6, and 7 are representative examples of a total of seven homozygous  
332 mutant and seven age-matched non-mutant animals that were examined by necropsy, and  
333 immunohistochemistry.

334

#### 335 *Whole genome sequencing and RNA-seq-based genotyping*

336 Whole genome sequencing was carried out on five animals from a single nuclear family for whom  
337 there was comprehensive information available regarding phenotype and breeding history: two  
338 affected individuals, their obligate carrier parents, and an obligate carrier sibling (based on  
339 affected offspring), as indicated in Figure S1. For RNA-seq, we used tissue from two of the same  
340 animals used for WGS (a sibling pair—one affected, one obligate carrier), and 14 additional  
341 animals: six affected, four obligate carriers (based on pedigree information, Figure S1), and four  
342 unaffected and unrelated individuals with no known connection to the pedigree (Table S1).

343 Genomic DNA was isolated from liver samples using a Qiagen DNeasy Blood & Tissue kit  
344 according to the manufacturer's instructions. DNA sequencing libraries were prepared for  
345 sequencing on the Illumina HiSeq X by the HudsonAlpha Genomic Services Lab by Covaris  
346 shearing, end repair, adapter ligation, and PCR using standard protocols. Library concentrations

347 were normalized using KAPA qPCR prior to sequencing. After sequencing, adapters were  
348 trimmed and FastQ files were quality checked using Trim Galore! 0.4.0 (a wrapper for cutadapt  
349 1.8.1 [27] and FastQC 0.10.1). Initially, trimmed reads were aligned using bwa 0.7.12 [28] to the  
350 Felis Catus 8.0 build. When it became available, reads were also aligned to the Felis Catus 9.0  
351 build. Most analyses were conducted with the Felis Catus 8.0 build because chain files for liftover  
352 from the 99 lives database were not available initially; however, analyses of candidate genes were  
353 carried out with the 9.0 build since this assembly has no gaps over the critical linkage region.  
354 Aligned reads were sorted and duplicates were marked with Picard tools 1.131. GATK 3.5.0 [29]  
355 was used for indel realignment, base quality recalibration, gVCF generation, and joint genotyping  
356 of genomic DNA. For RNA-seq data (described further below), variants were called using VarScan  
357 2.3.6 [30]. For the zygosity analysis depicted in Figure 3A, we required genotyping calls from at  
358 least 11/14 animals, to allow for contribution from regions with less coverage in some cats. snpEff  
359 4.1 [31] was used for annotation and filtering, and PROVEAN 1.1.5 [32] was used for missense  
360 damage prediction. For the *PEA15* frameshift, genotypes were confirmed by Sanger sequencing  
361 in 25 affected or obligate carrier animals.

362

### 363 *RNAseq and cell type deconvolution*

364 Total RNA was extracted from the grey matter of the cerebral cortex of 16 cats (seven affected  
365 cats, five obligate carriers based on breeding records, Figure S1, Table S1, and four unaffected  
366 animals from a different pedigree that did not segregate the cerebral dysgenesis mutation) using  
367 the Qiagen RNeasy Lipid Tissue Mini Kit according to the manufacturer's instructions. Ages  
368 ranged from four months to six years for affected cats, 2–12 years for obligate carriers, and 2–  
369 5.5 years for unaffected cats. RNA was treated with TURBO DNase, and RIN scores were  
370 measured using a BioAnalyzer. Libraries were generated using polyA selection and an Illumina  
371 Nextera RNA-Seq protocol. Library concentrations were normalized using KAPA qPCR prior to  
372 sequencing. Libraries were sequenced with paired end 50 bp reads on an Illumina HiSeq 2500.



373 Data from RNAseq was processed using aRNApipe [33], a python wrapper for several tools.  
374 Briefly, adapters were trimmed and FastQ files were quality checked using Trim Galore! 0.4.0 (a  
375 wrapper for cutadapt 1.8.1 [27] and FastQC 0.10.1). Reads were aligned with STAR 2.4.2a [34]  
376 to the Felis Catus 8.0 build and counted by gene with HTSeq 0.5.3 [35]. Count data were  
377 normalized and analyzed using DESeq2 [36] in R.

378 We collected RNA-seq data from 16 cats (7 homozygous mutant, 5 heterozygous, and 4  
379 homozygous non-mutant). For the homozygous mutant vs. non-mutant comparison depicted in  
380 Figure 8A, 6 cats were excluded: 3 homozygous mutant kittens, 1 heterozygous mutant that died  
381 from a generalized seizure, and 1 heterozygous mutant and 1 homozygous non-mutant that were  
382 outliers on principal component analysis (Figure S5). 10 cats (4 homozygous mutant, 3  
383 heterozygous mutant, and 3 homozygous non-mutant) remained for analysis. Transcripts were  
384 considered for cell type deconvolution analysis if they were at least two fold enriched over any  
385 other cell type with a raw p value of less than 0.2 using relative abundance described previously  
386 [14].

387

### 388 *Amplicon sequencing*

389 Amplicon sequencing was conducted for 96 cats, 91 with no previous genotype information along  
390 with one with genome sequencing and four with RNA-seq. Amplicons were chosen to span 26  
391 variants spaced along the ~70 Mb interval that contained the candidate region on chromosome  
392 F1 as determined by zygosity analysis (Figure 3A), 4 additional variants space along the  
393 remainder of chromosome F1, and 20 variants from other chromosomes. Primers used are listed  
394 in Table S5. After PCR with 1–2 primer pairs per reaction in 384-well plates, amplicons were  
395 pooled for each cat and barcoded for sequencing by ligating adapters to A-tails. Library  
396 concentrations were normalized using KAPA qPCR prior to sequencing. Amplicons were  
397 sequenced using an Illumina MiSeq with 150 bp paired end reads. After sequencing, adapters  
398 were trimmed and FastQ files were quality checked using Trim Galore! 0.4.0 (a wrapper for



399 cutadapt 1.8.1 [27] and FastQC 0.10.1). Trimmed reads were aligned using bwa 0.7.12 [28] to  
400 the Felis Catus 8.0 build. Picard tools 1.131 was used to sort, mark duplicates, and index.  
401 Platypus 0.8.1 [37] was used to call variants.

402

#### 403 *Haplotyping, LOD Score Calculation, and Other Analysis & Statistics*

404 Merlin 1.1.2 [38] was used for haplotyping and LOD score calculation (Table S3), according to a  
405 rare recessive model. Coverage was calculated using goleft indexcov 0.1.7 [39]. CNV analysis  
406 was conducted with Delly 0.7.8 [40]. Other packages used for standard processing of VCFs were  
407 vt [41], bcftools [42], and vcftools [43]. Liftover to hg38 for CADD [44] analysis was conducted  
408 with Crossmap 0.2.7 [45]. PEA15 conservation was assessed using a previously published  
409 sequence-to-structure-to-function workflow [46]. Other statistics were calculated in either R or  
410 Prism 7.

411

#### 412 *Histological and Immunohistochemical analysis*

413 Histological and immunohistochemical (IHC) analyses were performed on cats that ranged in age  
414 from 1–8 months with age-matched controls. Luxol fast blue (LFB) staining was performed as  
415 previously described [47] both with and without Cresyl-Echt violet counterstain.  
416 Immunohistochemical stains were performed using Dako automated immunostainer (Autostainer  
417 Link48, Dako-Agilent, Santa Clara, CA) using a low pH (6.1) antigen retrieval. IBA1 (Biocare  
418 Medical, CP290A; 1:100 dilution) and Olig2 (Abcam, EPR2678; 1:200 dilution) antibodies were  
419 incubated for 30 minutes. GFAP antibody (IR 52461-2 Dako-Agilent, Santa Clara, CA, no dilution)  
420 was incubated for 20 minutes. MAP2 antibody (Sigma-Aldrich, HM-2; 1:1000 dilution) was  
421 incubated for four hours. Detection was performed using the Dako EnVision HRP detection with  
422 DAB chromogen and hematoxylin counterstain. For quantification, slides were digitally scanned  
423 at 40x using an Aperio Scan Scope (Leica Biosystems, Buffalo Grove, IL, USA). Algorithms were  
424 written to quantify stained area of DAB for each individual IHC stain or LFB stain using Visiopharm

425 quantitative digital histopathology software (Visiopharm, Hoersholm Denmark) and applied to all  
426 slides of an individual stain, except MAP2 as MAP2 had broad cytoplasmic staining that did not  
427 allow for individual cell density assessment.

428

#### 429 *Magnetic Resonance Imaging*

430 MRI data were acquired as previously described on a seven Tesla MAGNETOM scanner  
431 (Siemens Healthcare, Erlangen, Germany) from adult affected (n=3), carrier (n=2) and unaffected  
432 (n=4) cats as previously described [48]. A 32-channel head coil (Nova Medical, Boston, Mass.)  
433 was used for all scans. Anatomical coronal images were acquired using 3D MPRAGE  
434 (Magnetization-PRepared RAPid Gradient Echo) with 0.5mm isotropic resolution and TR/TE of  
435 1910/2.5ms, followed by 2D axial T2 turbo spin echo (TSE) images with TR/TE of 5450/12ms and  
436 a resolution of (0.25x0.25x1) mm<sup>3</sup>. MRI data were analyzed with EFilm 3.2 software (Merge  
437 Healthcare, Chicago).

438

#### 439 *Immunoblot analysis*

440 Samples of feline cerebral cortex (5 – 10 mg) were homogenized in 400 µl of RIPA buffer  
441 (PIERCE, ThermoFisher, Waltham, MA, USA) with a hand-held micro-pestle for 30 sec, followed  
442 by passage through a 25G needle and kept on ice for 20 min. After centrifugation at 16,200 ×g  
443 for 30 min at 4°C, the soluble fraction was transferred to a new tube and total protein concentration  
444 was determined by DC protein assay (Bio-Rad, Hercules, CA, USA). Following quantification, 33  
445 µg of protein sample were mixed with 4× Laemmli sample buffer (Bio-Rad) containing 400mM  
446 Dithiothreitol. Protein fractions were separated with 18 % sodium dodecyl sulfate polyacrylamide  
447 gel electrophoresis, and transferred to Odyssey® nitrocellulose membrane (Li-Cor, Lincoln, NE,  
448 USA), blocked in LI-COR Odyssey blocking buffer (Lincoln, NE) for 1 h, and incubated with rabbit  
449 polyclonal anti-PEA-15 (C-terminal amino acids 93-123 of Human PEA15) antibody ab135694  
450 (Abcam, Cambridge, UK) at a concentration of 1:100 and anti-GAPDH antibody (MAB374, EMD

451 Millipore, Burlington, MA, USA) at a concentration of 1:500. Secondary antibodies (1:15,000) were  
452 IRDye®680RD Goat anti-Rabbit IgG (H+L, Li-Cor) and IRDye®800CW Goat anti-Mouse IgG  
453 (H+L, Li-Cor), respectively. The fluorescent signal was detected using Odyssey® Infrared imaging  
454 system (Li-Cor).

455

#### 456 *Primary skin fibroblast culture*

457 Primary fibroblasts were established from feline skin samples. Dulbecco's modified eagle's  
458 medium (DMEM, Corning, NY) supplemented with 10% fetal bovine serum (FBS), penicillin (100  
459 IU/ml), streptomycin (100 µg/ml), and amphotericin B (0.25 µg/ml) was used as a standard growth  
460 media. Briefly, collected skin pieces were placed with the connective tissue in direct contact with  
461 the culture surface and cultured in growth media for 5 to 7 days until visible colonies formed. After  
462 removing skin pieces, cells were further cultured in growth media or stored in liquid nitrogen in  
463 freezing media containing 10% dimethyl sulfoxide

464

#### 465 *Cell viability, caspase-8 activity, and cell proliferation assay*

466 Cell viability and caspase-8 activity were assessed in order to determine the susceptibility of  
467 primary fibroblasts to TNF-α induced apoptosis. Colorimetric Cell Viability Kit I (WST-8 reagent,  
468 PromoKine, Heidelberg, Germany) and Caspase-Glo® 8 Assay (Promega, Madison, WI) were  
469 used for cell viability assay and caspase-8 assay, respectively. In brief, cells were seeded in 96-  
470 well multiwell tissue culture plates at a density of 15,000 cells/90 µL/well. After 20 hours of  
471 incubation at 37 °C, cells were treated with 10 ng/ml purified recombinant human TNF-α  
472 (Peprotech, Rocky Hill, NJ) prepared in growth media containing 10 µg/ml of Actinomycin D (MP  
473 Biomedicals, Solon, OH). Two identical plates were prepared for each experiment. Following 3  
474 hours of TNF-α treatment, one plate was equilibrated to room temperature for 15 min, caspase-8  
475 assay substrate was added and the luminescent signal was evaluated by Infinite M200 microplate  
476 reader (Tecan, Mannedorf, Switzerland) after 30 minutes of room temperature incubation. The

477 other plate was cultured for 6 hours post TNF- $\alpha$  treatment. WST-8 reagent was added to each  
478 well and the plate was incubated at 37 °C for 1.5 hours. Then, the absorbance at 450 nm was  
479 measured by Infinite M200 microplate reader. Cell proliferation was assessed in primary  
480 fibroblasts as percent response to fibroblast growth factor-b (FGFb) relative to untreated cells  
481 from each individual. Cells were seeded in 6-well multiwell tissue culture plates at a density of  
482 90,000 cells/2 mL/well. After 20 hours of incubation at 37 °C, cells were treated with 20 ng/ml  
483 purified FGFb (Peprotech, Rocky Hill, NJ) prepared in growth media. Following 72 hours of FGFb  
484 treatment, cell were washed once with PBS(-) and dethatched with 0.25% trypsin-EDTA  
485 (Corning). The total cell number in each well was determined using trypan blue dye exclusion on  
486 a hemocytometer.

487

488

#### 489 *Data Availability*

490 All sequencing data are publicly available at SRA Project PRJNA495843. Descriptors for each  
491 sample are included at SRA, and also in the supplemental table (S1 Table).

492

#### 493 **Acknowledgements**

494 We thank Joseph Benito for technical assistance in generating RNA-seq libraries, Corneliu  
495 Henegar for assistance with computational scripts, Bandon Brunson for initial review of the  
496 histology, Edward Morrison for his review of the histopathology and guidance, Nancy Merner for  
497 her help with the pedigree, Matt Miller for reading and revising the manuscript, and Nancy  
498 Morrison for technical support in generating primary feline fibroblasts. 99 Lives Consortium  
499 members that contributed to the 99 Lives analysis used in this manuscript include: Reuben M.  
500 Buckley<sup>1</sup>, Danielle Aberdein<sup>2</sup>, Paulo C. Alves<sup>3,4</sup>, Rebecca R. Bellone<sup>5</sup>, Tomas F.  
501 Bergström<sup>6</sup>, Adam R. Boyko<sup>7</sup>, Jeffrey A. Brockman<sup>8</sup>, Margret L. Casal<sup>9</sup>, Marta G.

502 Castelhana<sup>10</sup>, Ottmar Distl<sup>11</sup>, Nicholas H. Dodman<sup>12</sup>, N. Matthew Ellinwood<sup>13</sup>, Jonathan  
503 E. Fogle<sup>14</sup>, Oliver P. Forman<sup>15</sup>, Dorian J. Garrick<sup>2,13</sup>, Edward I. Ginns<sup>16</sup>, Jens  
504 Häggström<sup>17</sup>, Robert J. Harvey<sup>18</sup>, Daisuke Hasegawa<sup>19</sup>, Bianca Haase<sup>20</sup>, Christopher R.  
505 Helps<sup>21</sup>, Isabel Hernandez<sup>22</sup>, Marjo K. Hytönen<sup>23</sup>, Daniel M. Ibrahim<sup>24-26</sup>, Maria  
506 Kaukonen<sup>23</sup>, Tomoki Kosho<sup>27</sup>, Emilie Leclerc<sup>2,28</sup>, Teri L. Lear<sup>29</sup>, Tosso Leeb<sup>30</sup>, Ronald  
507 H.L. Li<sup>31</sup>, Hannes Lohi<sup>23</sup>, Maria Longeri<sup>32</sup>, Dario G. Lupianez<sup>33</sup>, Mark A. Magnuson<sup>34</sup>,  
508 Richard Malik<sup>35</sup>, Shrinivas Mane<sup>36</sup>, John S. Munday<sup>2</sup>, William J. Murphy<sup>37</sup>, Niels C.  
509 Pedersen<sup>38</sup>, Simon M. Peterson-Jones<sup>39</sup>, Max F. Rothschild<sup>13</sup>, Clare Rusbridge<sup>40</sup>, Beth  
510 Shapiro<sup>41</sup>, Joshua A. Stern<sup>38</sup>, Orsolya Symmons<sup>42</sup>, William F. Swanson<sup>43</sup>, Karen A.  
511 Terio<sup>44</sup>, Rory J. Todhunter<sup>10</sup>, Wesley C. Warren<sup>45</sup>, Elizabeth A. Wilcox<sup>10</sup>, Julia H.  
512 Wildschutte<sup>46</sup>, Yoshihiko Yu<sup>19</sup>, and Leslie A. Lyons<sup>1</sup>.

513

514 <sup>1</sup>Department of Veterinary Medicine and Surgery, College of Veterinary Medicine,  
515 University of Missouri, Columbia, Missouri, 65211 USA

516 <sup>2</sup>School of Veterinary Biomedical Science, Massey University, Palmerston North 4442  
517 New Zealand

518 <sup>3</sup>CIBIO/InBIO, Centro de Investigação em Biodiversidade e Recursos Genéticos/InBIO  
519 Associate Lab & Faculdade de Ciências, Universidade do Porto, Campus e Vairão, 4485–  
520 661 Vila do Conde, Portugal

521 <sup>4</sup>Wildlife Biology Program, University of Montana, Missoula, Montana, 59812 USA

522 <sup>5</sup>Veterinary Genetics Laboratory, University of California, Davis, Davis California, 95616 USA

523 <sup>6</sup>Department of Animal Breeding and Genetics, Swedish University of Agricultural  
524 Sciences, 750 07 Uppsala, Sweden

525 <sup>7</sup>Department of Biomedical Sciences, College of Veterinary Medicine, Cornell University,  
526 Ithaca, New York, 14853 USA

527 <sup>8</sup>Hill's Pet Nutrition Inc., Topeka, Kansas 66601 USA

528 <sup>9</sup>Reproduction, and Pediatrics, School of Veterinary Medicine, University of Pennsylvania,  
529 Philadelphia, PA 19104 USA

530 <sup>10</sup>Department of Clinical Sciences, College of Veterinary Medicine, Cornell University,  
531 Ithaca, New York, 14853 USA

532 <sup>11</sup>Institute for Animal Breeding and Genetics, University of Veterinary Medicine Hannover  
533 (Foundation), 30559, Hannover, Germany

534 <sup>12</sup>Department of Clinical Sciences, Cummings School of Veterinary Medicine, Tufts  
535 University, Grafton, MA, 01536 USA

536 <sup>13</sup>Department of Animal Science, College of Agriculture and Life Sciences, Iowa State  
537 University, Ames, Iowa, 50011 USA

538 <sup>14</sup>College of Veterinary Medicine, North Carolina State University, Raleigh, NC 27607

539 <sup>15</sup>WALTHAM Centre for Pet Nutrition, Freeby Lane, Waltham on the Wolds,  
540 Leicestershire, LE14 4RT UK

541 <sup>16</sup>Department of Psychiatry, University of Massachusetts Medical School, Worcester, MA,  
542 01655 USA

543 <sup>17</sup>Department of Clinical Sciences, Faculty of Veterinary Medicine and Animal Science,  
544 Swedish University of Agricultural Sciences, Uppsala, SE-750 07 Sweden

545 <sup>18</sup>School of Health and Sport Sciences, University of the Sunshine Coast, Sippy Downs,  
546 QLD, Australia

547 <sup>19</sup>Department of Clinical Veterinary Medicine, Nippon Veterinary and Life Science  
548 University, Tokyo 180-8602 Japan

549 <sup>20</sup>Sydney School of Veterinary Science, Faculty of Science, University of Sydney, Sydney,  
550 NSW, 2006, Australia

551 <sup>21</sup>Langford Vets, University of Bristol, Langford, Bristol, BS40 5DU UK

552 <sup>22</sup>Pediatrics and Medical Genetics Service, College of Veterinary Medicine, Cornell  
553 University, Ithaca, New York, 14853 USA

554 <sup>23</sup>Department of Veterinary Biosciences; Department of Medical Genetics, University of  
555 Helsinki and Folkhälsan Research Center, Helsinki 00014 Finland

556 <sup>24</sup>Max Planck Institute for Molecular Genetics, 14195 Berlin, Germany

557 <sup>25</sup>Institute for Medical and Human Genetics, Charité Universitätsmedizin Berlin, 13353  
558 Berlin, Germany

559 <sup>26</sup>Berlin-Brandenburg Center for Regenerative Therapies, Charité-Universitätsmedizin  
560 Berlin, D 13353 Berlin, Germany.

561 <sup>27</sup>Department of Medical Genetics, Center for Medical Genetics, Shinshu University  
562 Hospital, Matsumoto, Nagano 390-8621, Japan

563 <sup>28</sup>SPF - Diana Pet food – Symrise Group – 56250 Elven, France

564 <sup>29</sup>Department of Veterinary Science, University of Kentucky - Lexington, Lexington, KY,  
565 40506 USA (*In memoriam*)

566 <sup>30</sup>Vetsuisse Faculty, Institute of Genetics, University of Bern, 3001 Bern, Switzerland

567 <sup>31</sup>Department of Surgical and Radiological Sciences, School of Veterinary Medicine,  
568 University of California Davis, One Shields Ave, Davis, CA, 95616 USA

569 <sup>32</sup>Dipartimento di Medicina Veterinaria, University of Milan, 20122 Milan, Italy

570 <sup>33</sup>Epigenetics and Sex Development Group, Berlin Institute for Medical Systems

571 Biology, Max-Delbrück Center for Molecular Medicine, Berlin-Buch, Germany.

572 <sup>34</sup>Departments of Molecular Physiology and Biophysics, Cell and Developmental

573 Biology, and Medicine, Vanderbilt University, School of Medicine, Nashville, Tennessee,

574 37232 USA

575 <sup>35</sup>Centre for Veterinary Education, University of Sydney, Sydney, NSW, 2006 Australia

576 <sup>36</sup>Elanco Animal Health, Greenfield, IN 46140 USA

577 <sup>37</sup>Department of Veterinary Integrative Biosciences, College of Veterinary Medicine,

578 Texas A&M University, College Station, Texas, 77845 USA

579 <sup>38</sup>Department of Medicine and Epidemiology, School of Veterinary Medicine, University

580 of California at Davis, Davis, California, 95616 USA

581 <sup>39</sup>Small Animal Clinical Sciences, College of Veterinary Medicine, Michigan State

582 University, East Lansing, Michigan, 48824 USA

583 <sup>40</sup>School of Veterinary Medicine, Faculty of Health & Medical Sciences, Univesity of

584 Surrey, Guildford, Surrey, GU2 7AL, United Kingdom

585 <sup>41</sup>Department of Ecology and Evolutionary Biology, University of California, Santa Cruz,

586 Santa Cruz, California 95064 USA

587 <sup>42</sup>Department of Bioengineering, University of Pennsylvania, Philadelphia, PA 19104,

588 USA

589 <sup>43</sup>Center for Conservation and Research of Endangered Wildlife (CREW), Cincinnati Zoo

590 & Botanical Garden, Cincinnati, Ohio, 45220 USA

591 <sup>44</sup>Zoological Pathology Program, University of Illinois, Brookfield, Illinois 60513 USA



592 <sup>45</sup>Division of Animal Sciences, College of Agriculture, Food and Natural Resources;  
593 School of Medicine, University of Missouri, Columbia, Missouri 65211, USA  
594 <sup>46</sup>Bowling Green State University, Department of Biological Sciences, Bowling Green,  
595 Ohio 43403 USA

596 **References:**

- 597 1. Schaefer GB, Sheth RD, Bodensteiner JB. Cerebral dysgenesis. An overview.  
598 Neurologic clinics. 1994;12(4):773–88. Epub 1994/11/01. PubMed PMID: 7845342.
- 599 2. Parrini E, Conti V, Dobyns WB, Guerrini R. Genetic Basis of Brain Malformations.  
600 Molecular syndromology. 2016;7(4):220–33. Epub 2016/10/27. doi: 10.1159/000448639.  
601 PubMed PMID: 27781032; PubMed Central PMCID: PMC5073505.
- 602 3. Poirier K, Lebrun N, Broix L, Tian G, Saillour Y, Boscheron C, et al. Mutations in TUBG1,  
603 DYNC1H1, KIF5C and KIF2A cause malformations of cortical development and microcephaly.  
604 Nat Genet. 2013;45(6):639–47. Epub 2013/04/23. doi: 10.1038/ng.2613. PubMed PMID:  
605 23603762; PubMed Central PMCID: PMC3826256.
- 606 4. Defelipe J. The evolution of the brain, the human nature of cortical circuits, and  
607 intellectual creativity. Front Neuroanat. 2011;5:29. Epub 2011/06/08. doi:  
608 10.3389/fnana.2011.00029. PubMed PMID: 21647212; PubMed Central PMCID:  
609 PMC3098448.
- 610 5. Sun T, Hevner RF. Growth and folding of the mammalian cerebral cortex: from  
611 molecules to malformations. Nat Rev Neurosci. 2014;15(4):217–32. Epub 2014/03/22. doi:  
612 10.1038/nrn3707. PubMed PMID: 24646670; PubMed Central PMCID: PMC4107216.
- 613 6. Gregory MD, Kippenhan JS, Dickinson D, Carrasco J, Mattay VS, Weinberger DR, et al.  
614 Regional Variations in Brain Gyrification Are Associated with General Cognitive Ability in  
615 Humans. Curr Biol. 2016;26(10):1301–5. Epub 2016/05/03. doi: 10.1016/j.cub.2016.03.021.  
616 PubMed PMID: 27133866; PubMed Central PMCID: PMC4879055.
- 617 7. Matsumoto N, Shinmyo Y, Ichikawa Y, Kawasaki H. Gyrification of the cerebral cortex  
618 requires FGF signaling in the mammalian brain. Elife. 2017;6. Epub 2017/11/15. doi:  
619 10.7554/eLife.29285. PubMed PMID: 29132503; PubMed Central PMCID: PMC5685484.
- 620 8. Shinmyo Y, Terashita Y, Dinh Duong TA, Horiike T, Kawasumi M, Hosomichi K, et al.  
621 Folding of the Cerebral Cortex Requires Cdk5 in Upper-Layer Neurons in Gyrencephalic

- 622 Mammals. *Cell Rep.* 2017;20(9):2131–43. Epub 2017/08/31. doi: 10.1016/j.celrep.2017.08.024.  
623 PubMed PMID: 28854363.
- 624 9. Griffin BBHJ. *Domestic Cats as Laboratory Animal Models*. 2nd ed. Fox JG, editor:  
625 Academic Press; 2002. 22 p.
- 626 10. Gurda BL, Bradbury AM, Vite CH. *Canine and Feline Models of Human Genetic*  
627 *Diseases and Their Contributions to Advancing Clinical Therapies*. *Yale J Biol Med.*  
628 2017;90(3):417–31. Epub 2017/09/29. PubMed PMID: 28955181; PubMed Central PMCID:  
629 PMCPMC5612185.
- 630 11. Martin DR, Cox NR, Morrison NE, Kennamer DM, Peck SL, Dodson AN, et al. Mutation  
631 of the GM2 activator protein in a feline model of GM2 gangliosidosis. *Acta Neuropathol.*  
632 2005;110(5):443–50. Epub 2005/10/04. doi: 10.1007/s00401-005-1040-6. PubMed PMID:  
633 16200419.
- 634 12. Jezyk PF, Haskins ME, Patterson DF, Mellman WJ, Greenstein M.  
635 *Mucopolysaccharidosis in a cat with arylsulfatase B deficiency: a model of Maroteaux-Lamy*  
636 *syndrome*. *Science.* 1977;198(4319):834–6. Epub 1977/11/25. doi: 10.1126/science.144321.  
637 PubMed PMID: 144321.
- 638 13. Lyons LA, Creighton EK, Alhaddad H, Beale HC, Grahn RA, Rah H, et al. Whole  
639 genome sequencing in cats, identifies new models for blindness in *AIPL1* and somite  
640 segmentation in *HES7*. *BMC Genomics.* 2016;17:265. Epub 2016/04/01. doi: 10.1186/s12864-  
641 016-2595-4. PubMed PMID: 27030474; PubMed Central PMCID: PMCPMC4815086.
- 642 14. Zhang Y, Chen K, Sloan SA, Bennett ML, Scholze AR, O'Keeffe S, et al. An RNA-  
643 sequencing transcriptome and splicing database of glia, neurons, and vascular cells of the  
644 cerebral cortex. *J Neurosci.* 2014;34(36):11929–47. doi: 10.1523/JNEUROSCI.1860-14.2014.  
645 PubMed PMID: 25186741; PubMed Central PMCID: PMCPMC4152602.
- 646 15. Kitsberg D, Formstecher E, Fauquet M, Kubes M, Cordier J, Canton B, et al. Knock-out  
647 of the neural death effector domain protein PEA-15 demonstrates that its expression protects

- 648 astrocytes from TNFalpha-induced apoptosis. *J Neurosci.* 1999;19(19):8244–51. Epub  
649 1999/09/24. PubMed PMID: 10493725.
- 650 16. Ascione F, Vasaturo A, Caserta S, D'Esposito V, Formisano P, Guido S. Comparison  
651 between fibroblast wound healing and cell random migration assays in vitro. *Experimental cell*  
652 *research.* 2016;347(1):123–32. Epub 2016/08/01. doi: 10.1016/j.yexcr.2016.07.015. PubMed  
653 PMID: 27475838.
- 654 17. Buonomo R, Giacco F, Vasaturo A, Caserta S, Guido S, Pagliara V, et al. PED/PEA-15  
655 controls fibroblast motility and wound closure by ERK1/2-dependent mechanisms. *J Cell*  
656 *Physiol.* 2012;227(5):2106–16. Epub 2011/07/23. doi: 10.1002/jcp.22944. PubMed PMID:  
657 21780113; PubMed Central PMCID: PMC3306794.
- 658 18. Renault F, Formstecher E, Callebaut I, Junier MP, Chneiweiss H. The multifunctional  
659 protein PEA-15 is involved in the control of apoptosis and cell cycle in astrocytes. *Biochem*  
660 *Pharmacol.* 2003;66(8):1581–8. Epub 2003/10/14. PubMed PMID: 14555237.
- 661 19. Estelles A, Yokoyama M, Nothias F, Vincent JD, Glowinski J, Vernier P, et al. The major  
662 astrocytic phosphoprotein PEA-15 is encoded by two mRNAs conserved on their full length in  
663 mouse and human. *J Biol Chem.* 1996;271(25):14800–6. Epub 1996/06/21. PubMed PMID:  
664 8662970.
- 665 20. Danziger N, Yokoyama M, Jay T, Cordier J, Glowinski J, Chneiweiss H. Cellular  
666 expression, developmental regulation, and phylogenic conservation of PEA-15, the astrocytic  
667 major phosphoprotein and protein kinase C substrate. *J Neurochem.* 1995;64(3):1016–25. Epub  
668 1995/03/01. PubMed PMID: 7861130.
- 669 21. Formisano P, Ragno P, Pesapane A, Alfano D, Alberobello AT, Rea VE, et al.  
670 PED/PEA-15 interacts with the 67 kD laminin receptor and regulates cell adhesion, migration,  
671 proliferation and apoptosis. *J Cell Mol Med.* 2012;16(7):1435–46. Epub 2011/09/08. doi:  
672 10.1111/j.1582-4934.2011.01411.x. PubMed PMID: 21895963; PubMed Central PMCID:  
673 PMC3823213.

- 674 22. Mace PD, Wallez Y, Egger MF, Dobaczewska MK, Robinson H, Pasquale EB, et al.  
675 Structure of ERK2 bound to PEA-15 reveals a mechanism for rapid release of activated MAPK.  
676 Nat Commun. 2013;4:1681. Epub 2013/04/12. doi: 10.1038/ncomms2687. PubMed PMID:  
677 23575685; PubMed Central PMCID: PMC3640864.
- 678 23. Exler RE, Guo X, Chan D, Livne-Bar I, Vicic N, Flanagan JG, et al. Biomechanical insult  
679 switches PEA-15 activity to uncouple its anti-apoptotic function and promote erk mediated tissue  
680 remodeling. Experimental cell research. 2016;340(2):283–94. Epub 2015/12/01. doi:  
681 10.1016/j.yexcr.2015.11.023. PubMed PMID: 26615958.
- 682 24. Fiory F, Spinelli R, Raciti GA, Parrillo L, D'Esposito V, Formisano P, et al. Targetting  
683 PED/PEA-15 for diabetes treatment. Expert Opin Ther Targets. 2017;21(6):571–81. Epub  
684 2017/04/12. doi: 10.1080/14728222.2017.1317749. PubMed PMID: 28395542.
- 685 25. Ramos JW, Townsend DA, Piarulli D, Kolata S, Light K, Hale G, et al. Deletion of PEA-  
686 15 in mice is associated with specific impairments of spatial learning abilities. BMC  
687 neuroscience. 2009;10:134. Epub 2009/11/18. doi: 10.1186/1471-2202-10-134. PubMed PMID:  
688 19917132; PubMed Central PMCID: PMC3640864.
- 689 26. Lek M, Karczewski KJ, Minikel EV, Samocha KE, Banks E, Fennell T, et al. Analysis of  
690 protein-coding genetic variation in 60,706 humans. Nature. 2016;536(7616):285–91. doi:  
691 10.1038/nature19057. PubMed PMID: 27535533; PubMed Central PMCID: PMC3640864.
- 692 27. Martin M. Cutadapt removes adapter sequences from high-throughput sequencing  
693 reads. EMBnet journal. 2011;17(1):pp. 10–2.
- 694 28. Li H, Durbin R. Fast and accurate short read alignment with Burrows–Wheeler  
695 transform. Bioinformatics. 2009;25(14):1754–60.
- 696 29. McKenna A, Hanna M, Banks E, Sivachenko A, Cibulskis K, Kernytsky A, et al. The  
697 Genome Analysis Toolkit: a MapReduce framework for analyzing next-generation DNA  
698 sequencing data. Genome res. 2010;20(9):1297–303.

- 699 30. Koboldt DC, Zhang Q, Larson DE, Shen D, McLellan MD, Lin L, et al. VarScan 2:  
700 somatic mutation and copy number alteration discovery in cancer by exome sequencing.  
701 *Genome res.* 2012;22(3):568–76.
- 702 31. Cingolani P, Platts A, Wang LL, Coon M, Nguyen T, Wang L, et al. A program for  
703 annotating and predicting the effects of single nucleotide polymorphisms, SnpEff: SNPs in the  
704 genome of *Drosophila melanogaster* strain w1118; iso-2; iso-3. *Fly.* 2012;6(2):80–92.
- 705 32. Choi Y, Chan AP. PROVEAN web server: a tool to predict the functional effect of amino  
706 acid substitutions and indels. *Bioinformatics.* 2015;31(16):2745–7.
- 707 33. Alonso A, Lasseigne BN, Williams K, Nielsen J, Ramaker RC, Hardigan AA, et al.  
708 aRNApipe: a balanced, efficient and distributed pipeline for processing RNA-seq data in high-  
709 performance computing environments. *Bioinformatics.* 2017;33(11):1727–9.
- 710 34. Dobin A, Davis CA, Schlesinger F, Drenkow J, Zaleski C, Jha S, et al. STAR: ultrafast  
711 universal RNA-seq aligner. *Bioinformatics.* 2013;29(1):15–21.
- 712 35. Anders S, Pyl PT, Huber W. HTSeq—a Python framework to work with high-throughput  
713 sequencing data. *Bioinformatics.* 2015;31(2):166–9.
- 714 36. Love MI, Huber W, Anders S. Moderated estimation of fold change and dispersion for  
715 RNA-seq data with DESeq2. *Genome Biol.* 2014;15(12):550.
- 716 37. Rimmer A, Phan H, Mathieson I, Iqbal Z, Twigg SR, Wilkie AO, et al. Integrating  
717 mapping-, assembly- and haplotype-based approaches for calling variants in clinical sequencing  
718 applications. *Nat Genet.* 2014;46(8):912.
- 719 38. Abecasis GR, Cherny SS, Cookson WO, Cardon LR. Merlin—rapid analysis of dense  
720 genetic maps using sparse gene flow trees. *Nat Genet.* 2002;30(1):97.
- 721 39. Pedersen BS, Collins RL, Talkowski ME, Quinlan AR. Indexcov: fast coverage quality  
722 control for whole-genome sequencing. *GigaScience.* 2017.

- 723 40. Rausch T, Zichner T, Schlattl A, Stütz AM, Benes V, Korbel JO. DELLY: structural  
724 variant discovery by integrated paired-end and split-read analysis. *Bioinformatics*.  
725 2012;28(18):i333–i9.
- 726 41. Tan A, Abecasis GR, Kang HM. Unified representation of genetic variants.  
727 *Bioinformatics*. 2015;31(13):2202–4. Epub 2015/02/24. doi: 10.1093/bioinformatics/btv112.  
728 PubMed PMID: 25701572; PubMed Central PMCID: PMC4481842.
- 729 42. Li H, Handsaker B, Wysoker A, Fennell T, Ruan J, Homer N, et al. The sequence  
730 alignment/map format and SAMtools. *Bioinformatics*. 2009;25(16):2078–9.
- 731 43. Danecek P, Auton A, Abecasis G, Albers CA, Banks E, DePristo MA, et al. The variant  
732 call format and VCFtools. *Bioinformatics*. 2011;27(15):2156–8.
- 733 44. Kircher M, Witten DM, Jain P, O'Roak BJ, Cooper GM, Shendure J. A general  
734 framework for estimating the relative pathogenicity of human genetic variants. *Nat Genet*.  
735 2014;46(3):310–5. doi: 10.1038/ng.2892. PubMed PMID: 24487276; PubMed Central PMCID:  
736 PMC3992975.
- 737 45. Zhao H, Sun Z, Wang J, Huang H, Kocher J-P, Wang L. CrossMap: a versatile tool for  
738 coordinate conversion between genome assemblies. *Bioinformatics*. 2013;30(7):1006–7.
- 739 46. Prokop JW, Lazar J, Crapitto G, Smith DC, Worthey EA, Jacob HJ. Molecular modeling  
740 in the age of clinical genomics, the enterprise of the next generation. *J Mol Model*.  
741 2017;23(3):75. Epub 2017/02/17. doi: 10.1007/s00894-017-3258-3. PubMed PMID: 28204942;  
742 PubMed Central PMCID: PMC5529140.
- 743 47. Luna LG. *Manual of Histologic Staining Methods of the Armed Forces Institute of*  
744 *Pathology*.: Blakiston Division, McGraw-Hill; 1968.
- 745 48. Gray-Edwards HL, Regier DS, Shirley JL, Randle AN, Salibi N, Thomas SE, et al. Novel  
746 Biomarkers of Human GM1 Gangliosidosis Reflect the Clinical Efficacy of Gene Therapy in a  
747 Feline Model. *Molecular therapy : the journal of the American Society of Gene Therapy*.

748 2017;25(4):892–903. Epub 2017/02/27. doi: 10.1016/j.ymthe.2017.01.009. PubMed PMID:

749 28236574; PubMed Central PMCID: PMC5383552.

750

751

752



753 **Table 1: Variants in coding sequence in the linkage region not present in the 99**  
754 **Lives dataset.** Note that two of the variants are synonymous in genes not expressed in  
755 brain. Of the two variants that change coding sequence, the missense variant in *LY9* is  
756 not predicted to be damaging, and *LY9* is not expressed in brain. In contrast, the  
757 frameshift variant in *PEA15* is predicted to be highly damaging, and *PEA15* is  
758 expressed a high level in brain.  
759  
760  
761  
762

Gene	Transcript	HGVS DNA	HGVS Protein	Protein Change	CADD	GERP	Cat Brain CPM	Human Brain CPM
LY9	XM_019822310.1	c.654A>G	p.Pro218Pro	Synonymous	0.0	-5.0	2.4	0.2
LY9	XM_019822310.1	c.478A>G	p.Met160Val	Missense	0.0	-7.9	2.4	0.2
PEA15	XM_023247767.1	c.176delA	p.Asn59fs	Frameshift	29.7	5.5	400.8	1087
ATP1A4	XM_023247847.1	c.1818C>T	p.Ala606Ala	Synonymous	NA (Hum. Ref.=A)		3.1	0.1

763 **Figure Legends**

764 **Figure 1. Affected cats have marked microcephaly with polymicrogyria.** Images of whole  
765 brain from (A) adult unaffected (+/+), and (B) adult and (C) juvenile affected (-/-) cats. Affected  
766 cats have dramatically decreased cerebral cortex size with normal formation of the cerebellum.  
767 (D) Brain weights of affected cats are significantly decreased with or without normalization to body  
768 weight, which is similar to unaffected cats. (E) Representative sections (left image, normal; right  
769 image, affected) from the region of the parietal cortex have gyrification defects characterized by  
770 shallow sulci and fusion of small gyri consistent with polymicrogyria, as well as abnormal white  
771 matter of the corona radiata and internal capsule.

772

773 **Figure 2. Changes in MRI are consistent with microcephaly and attenuation of gyral**  
774 **formation.** (A) Selected images from the frontoparietal region demonstrate marked attenuation  
775 and loss of gyral formation and white matter. Note the blurring of gray and white matter  
776 boundaries, especially apparent in the corona radiata. (B) Magnified region within the white box  
777 highlights the severe attenuation of the (C) anterior cingulate gyrus, outlined in white.

778

779 **Figure 3. Zygosity mapping, linkage, and haplotype analysis identifies a frameshift in**  
780 ***PEA15* as the cause of cerebral dysgenesis.** (A) Zygosity mapping, identifying all variants that  
781 are homozygous in 8 affected animals and heterozygous in 6 obligate carriers. Variants cluster in  
782 a region on the distal end of chromosome F1. (B) Diplotypes of 49 cats according to disease  
783 status as indicated. 13 diplotypes were imputed from progeny: the top 4 diplotypes are founders  
784 (note uncertain haplotype, denoted by X's), the next 5 diplotypes are for the next generation after  
785 the founders, and 4 other cats throughout the pedigree were imputed because a sample was not  
786 available. In the unaffected genotyped block, the cat indicated with a > is a cat that has 2 normal  
787 diplotypes but is present in the analysis because it was bred with a cat homozygous for the

788 disease diplotype. All affected animals are homozygous for a 1.3 Mb region (dashed black lines)  
789 **(C)** Linkage analysis confirms that the 1.3 Mb region on chromosome F1 identified by zygosity  
790 and haplotype analysis cosegregates with cerebral dysgenesis (coordinates given according to  
791 Felcat8). **(D)** CADD scores for all variants in the 1.3 Mb critical region that are homozygous in  
792 affected cats and absent from the 99 Lives dataset. Only 4 coding variants are present (see detail  
793 in **Table 1**). The 2 variants in *LY9* (not expressed in brain) are overlapping in the lower left corner.  
794 The 1 synonymous coding variant in *ATP1A4* (not expressed in brain) does not have a CADD  
795 score because the alternate allele is reference in human and therefore is not plotted here. The  
796 final coding variant in the region is a frameshift in *PEA15*, which is highly expressed in brain. The  
797 variant is predicted to be highly damaging by CADD.

798

799

800 **Figure 4. The *PEA15* mutation introduces a premature termination codon, and *PEA15***  
801 **protein is absent in affected cats. (A)** Map of *PEA15* demonstrating the mutation location near  
802 the beginning of Exon 2. **(B)** Overall levels of *PEA15* transcripts measured by RNA-Seq are  
803 decreased in cats homozygous for the *PEA15* mutation (One-way ANOVA  $*p < 0.0001$ ,  $*p < 0.01$   
804 by Tukey's *post hoc*). **(C)** Reads from the mutant *PEA15* allele in heterozygous cats are  
805 significantly reduced compared to non-mutant reads, while heterozygous variants in nearby genes  
806 do not exhibit allele bias (One-way ANOVA  $*p < 0.0001$ ,  $*p < 0.001$  by Tukey's *post hoc* vs. all of 3  
807 nearby genes comparing the % variant reads per cat as the unit of comparison with 24 to >3,000  
808 reads contributing to each % measurement for each gene). **(D)** *PEA15* is absent from affected  
809 animals by western blot.

810

811 **Figure 5. Affected cats have a significant loss of white matter. (A)** Subgross sections of  
812 MAP2 stained neurons highlight the variable decrease in cortical thickness, and the reduced

813 area of the corona radiata (arrows) and internal capsule. **(B)** Subgross sections of Luxol fast  
814 blue (LFB) stained for myelin indicates decreased white matter, **(C)** which is confirmed through  
815 quantification of LFB stained sections of the frontopareital region.

816

817 **Figure 6. Affected cats have loss of normal cerebral cortical layering, increased grey**  
818 **matter astrocytosis, and abnormal neuronal and axonal orientation. (A)** Photomicrographs  
819 of Luxol fast blue – Cresyl Echt Violet (LFB-CEV) stained sections depicting vertical columns in  
820 the parietal region of unaffected (left) and age-matched affected (right) cats. In unaffected cats, 6  
821 cortical layers extend from below the meninges (beginning with layer I, molecular layer) to the  
822 white matter (WM). In affected cats, grey matter thickness and column morphology are altered  
823 with disorganized layering. **(B)** Photomicrographs of GFAP stained sections of vertical columns  
824 reveals that affected cats exhibit a relative astrocytosis. Dotted lines indicate separation of white  
825 matter and grey matter. **(C)** Photomicrographs from MAP2 stained sections taken at  
826 approximately layers IV and V. Unaffected cats have linear axonal projections oriented  
827 perpendicular to the cortical meningeal surface while affected cats lack axonal directionality (bar  
828 = 20uM). In all images, the meningeal edge is located at the top.

829

830 **Figure 7. Affected cats have significantly increased astrocyte density within the grey**  
831 **matter. (A-B)** GFAP immunohistochemistry (IHC) of grey matter indicates increased density of  
832 astrocytes. **(C-E)** Digital image-analysis algorithms measured a significant increase in GFAP  
833 stain density primarily in grey matter stain. **(F-J)** Olig-2 staining indicates no significant change  
834 in the density of oligodendrocytes in grey matter, though an insignificant decrease of ~30% was  
835 noted in white matter. **(K-L)** No significant change in the density or morphology of microglia was  
836 detected in affected cats. **(M-O)** Microglial density findings are confirmed on quantification of IBA-  
837 1 stain. (bar = 200um)

838

839 **Figure 8. Differential expression analysis. (A)** Log<sub>2</sub>-fold change vs. magnitude of gene  
840 expression for homozygous mutant (M–mutant) (n=4) vs all unaffected (N&C–normal and  
841 carrier) (n=6) (heterozygous mutant (C–carrier) (n=3) and homozygous non-mutant (N–normal)  
842 (n=3)). Genes with a significant difference for the strict criteria of significance in both  
843 homozygous mutant (n=4) vs all unaffected (n=6) and homozygous mutant (n=4) vs  
844 homozygous non-mutant (n=3) are labeled (triangles). Data was collected for an additional 6  
845 animals, but excluded because of age, cause of death, or principal component analysis results  
846 **(Methods; Table S4; Figure S5).** **(B)** Quantitative changes in collagen gene expression for  
847 homozygous mutant, heterozygous, and homozygous non-mutant animals. No differences  
848 ( $p=0.61$ , two-way ANOVA) were detected between normal and carrier cats.

849

850 **Figure 9. Differences in levels of cell type–specific transcripts suggest altered cellular**  
851 **composition in the brains of affected cats. (A)** Oligodendrocyte precursor cell–specific  
852 transcripts are increased in affected cats (Two-way ANOVA  $*p<0.0001$  genotype effect). **(B)**  
853 Oligodendrocyte–specific transcripts are decreased in affected cats (Two-way ANOVA  $*p<0.0001$   
854 genotype effect). **(C)** Astrocyte–specific transcripts are increased in affected cats (Two-way  
855 ANOVA  $*p<0.0001$  genotype effect). **(D)** Endothelial cell–specific transcripts are increased in  
856 affected cats (Two-way ANOVA  $*p<0.0001$  genotype effect). **(E)** Neuron–specific transcripts did  
857 not change significantly (Two-way ANOVA  $p=0.60$  genotype effect). **(F)** Microglia–specific  
858 transcripts did not change significantly (Two-way ANOVA  $p=0.52$  genotype effect).

859

860 **Figure 10. Differences in cytokine-mediated apoptosis and proliferation in affected**  
861 **fibroblasts.** When treated with TNF $\alpha$ , there is **(A)** a significant decrease in cell viability and **(B)**  
862 a significant increase in caspase-8 activity of primary dermal fibroblasts from affected cats  
863 compared to unaffected cats. **(C)** When treated with 20ng/mL FGFb, proliferation is significantly

864 increased in primary dermal fibroblasts from affected cats compared to unaffected cats. There  
865 was no significant difference of untreated cells for either genotype.

866

867 **Figure 11. Hypothesized mechanisms of PEA15 mediated cerebral dysgenesis in domestic**  
868 **cats.** Beginning in late gestation through the early post-natal period of normal animals, there is  
869 increased neuronal apoptosis during synaptic pruning. PEA15, which is normally expressed at  
870 this time in the brain, protects from excessive apoptosis of neurons and inhibits proliferation of  
871 stimulated astrocytes. Therefore, loss of PEA15 is expected to cause increased neuronal  
872 apoptosis and increased proliferation of astrocytes. Grey matter astrocytosis may be a direct  
873 response to the increased apoptosis of neurons (reactive astrocytosis), and/or and excessive  
874 proliferation due to loss of PEA15 function. Abundant astrocytes produce excessive extracellular  
875 matrix which can form perineuronal nets and cause a premature end of the critical period for  
876 synaptic plasticity. These changes in development result in disorganized axonal development and  
877 underdeveloped white matter tracts which manifest as cerebral dysgenesis.

878

879

## 880 **Supporting Information**

881

882 **S1 Table. Table of cats from the GM2A and MPSVI breeding colonies where the cerebral**  
883 **dysgenesis mutation was identified.** Affected status is denoted by color with unaffected  
884 in white, obligate carriers based on breeding in grey, and affected cats in black.

885

886 **S2 Table. Cerebrospinal Fluid Analysis.** Cerebrospinal fluid protein concentration and cell  
887 counts in affected and carrier cats with a reference interval based on normal cats that was  
888 established by the Auburn University small animal teaching hospital.

889

890 **S3 Table. Haplotyping and LOD Score Calculation.** Merlin 1.1.2 was used for haplotyping  
891 and LOD score calculation. LOD score was calculated using parametric linkage analysis  
892 assuming a rare recessive model. Each marker is considered independently, equivalent to a theta  
893 value of zero. Note that, while we focused genotyping on chromosome F1 based on homozygosity  
894 mapping, we selectively genotyped a handful of markers on other chromosomes.

895

896 **S4 Table. RNA-seq counts and differentially expressed genes.** See excel file.

897 Summary statistics are listed for each gene, and counts per million are listed for each  
898 cat, with exclusion criteria for cats not included in summary statistics noted.

899

900 **S5 Table. Primer pairs for amplicon sequencing.** Note that multiple primer pairs were  
901 included for the top nominated region to maximize genotyping success and increase  
902 coverage. The *PEA15* frameshift site is bolded.

903

904

905 **S1 Fig. Pedigree.** Phenotype is denoted by color and indicated on the pedigree with  
906 unaffected in white, obligate carriers with a central dot, and homozygous mutant cats in  
907 black.

908

909 **S2 Fig. Cerebrospinal fluid enzyme activity.** (A) Changes in aspartate amino transferase  
910 and (B) lactate dehydrogenase enzyme activity in adult cats (n = 3) from the cerebral dysgenesis  
911 cohort.

912

913 **S3 Fig. FelCat9 coverage.** (A) When averaged over 10,000 base pair windows, coverage stays  
914 above 30x for all cats across the window linked to the phenotype. (B) When averaged over 1,000  
915 base pair windows, only a few regions dip below 20x coverage. (C) Regions with less than 20x  
916 coverage in all 5 cats. Note that regions are either in repetitive intronic or intergenic regions.

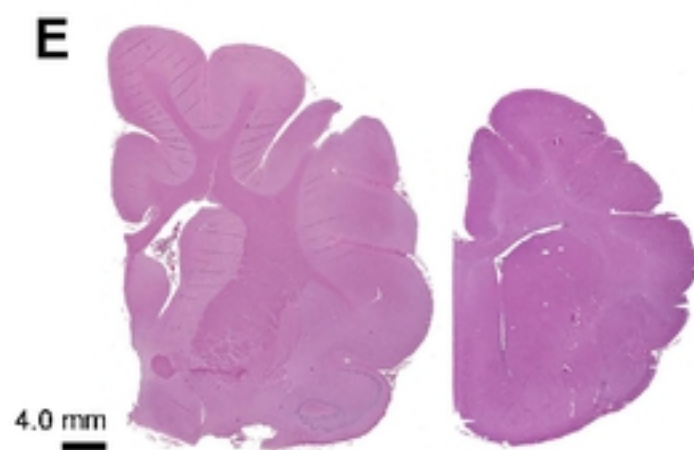
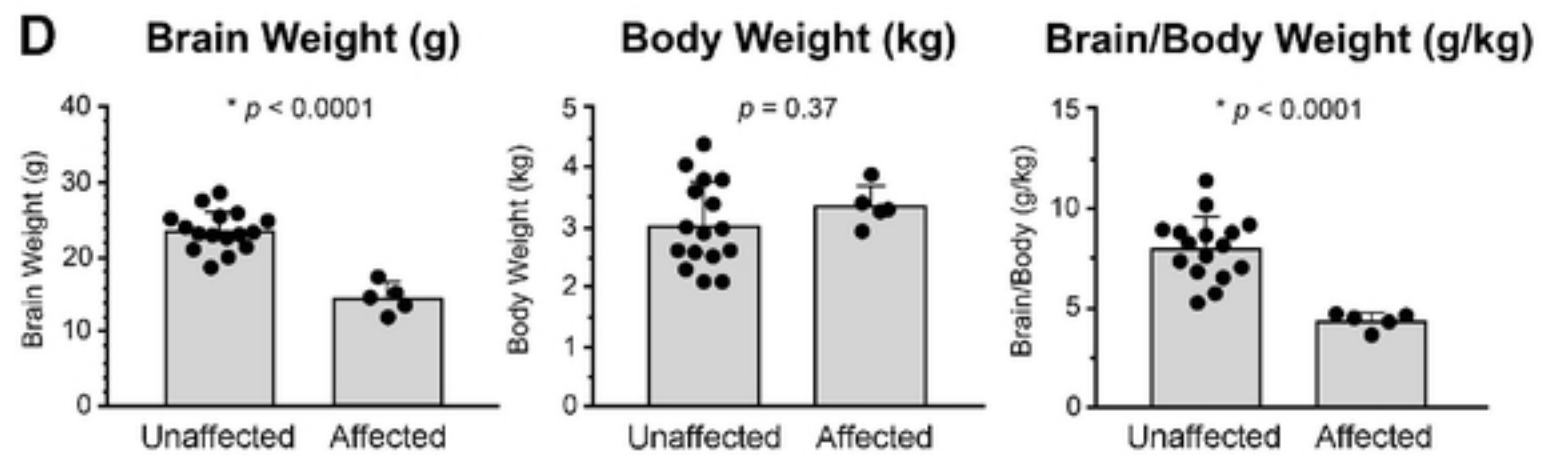
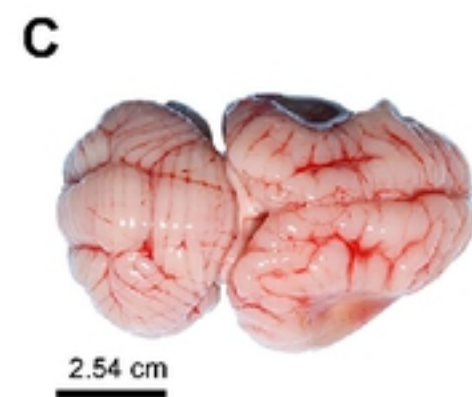
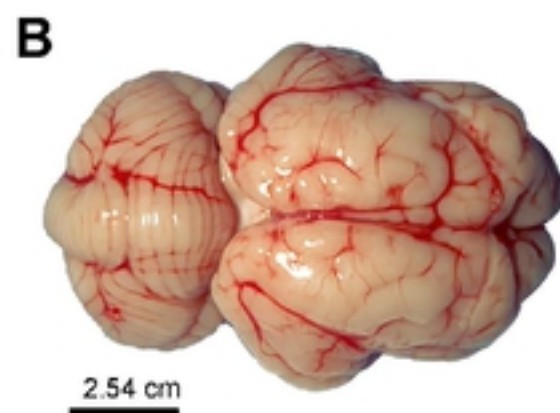
917

918 **S4 Fig. PEA15 Conservation.** (A) Conservation of PEA15 gene sequence was performed  
919 using the open reading frames from 150 species. Scores at each codon were assessed, where  
920 100% conservation corresponds to a score of 1, and this score also receives the addition of 0 if  
921 dN-dS of the site is below the mean, addition of 0.25 for sites with values above the mean to 1  
922 standard deviation above the mean, addition of 0.5 for sites greater than 1 standard deviation  
923 but below 2 standard deviations, and addition of 1 for sites greater than 2 standard deviations.  
924 Therefore, a score of 2 is maximal suggesting an amino acid that is 100% conserved with codon  
925 wobble indicative of a high selection rate at the position. (B) Conservation values were placed  
926 on a 21-codon sliding window (combining values for 10 codons before and after each position)  
927 to identify conserved motifs within the gene. (C) Model of PEA15 protein with a structural z-  
928 score of 0.12 (assessed with YASARA2 knowledge-based force field) suggesting accurate  
929 predictions of fold space. Colors are based on 150 species alignments fed into ConSurf.

930

931 **S5 Fig. Principal component analysis (PCA) of RNA-seq data from cat cortex.** Out of 16  
932 original cats, 1 cat was excluded from further analysis because of death by grand mal seizure,  
933 evident by PCA. 3 cats were excluded from further analysis because they were kittens to avoid  
934 detection of developmental false positive signals in differential expression analysis (1 kitten was  
935 also an outlier by PCA). 2 cats were excluded on the basis of being clear outliers by PCA. 10  
936 cats (4 homozygous mutant, 3 heterozygous mutant, and 3 homozygous non-mutant) remained  
937 for analysis.



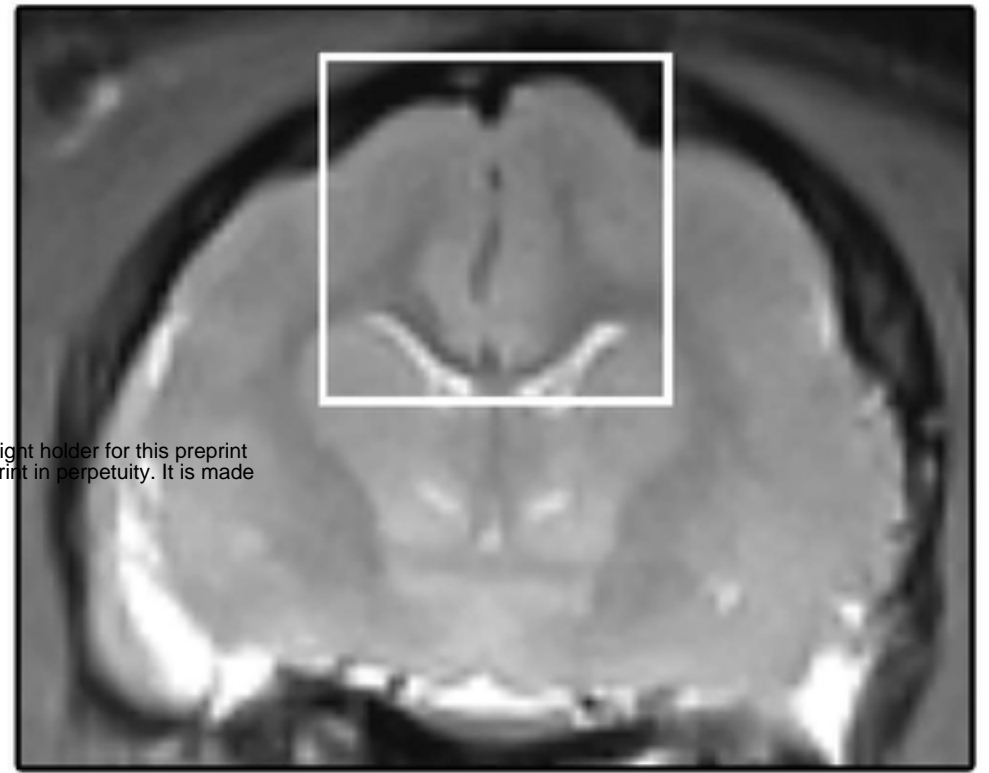
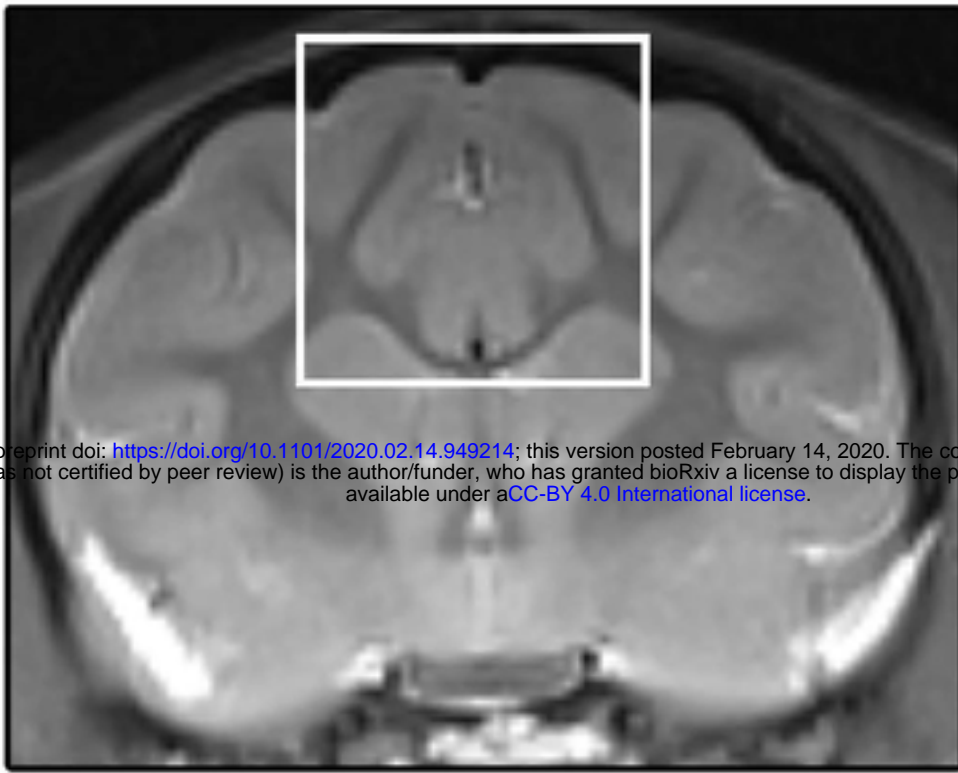


# Unaffected

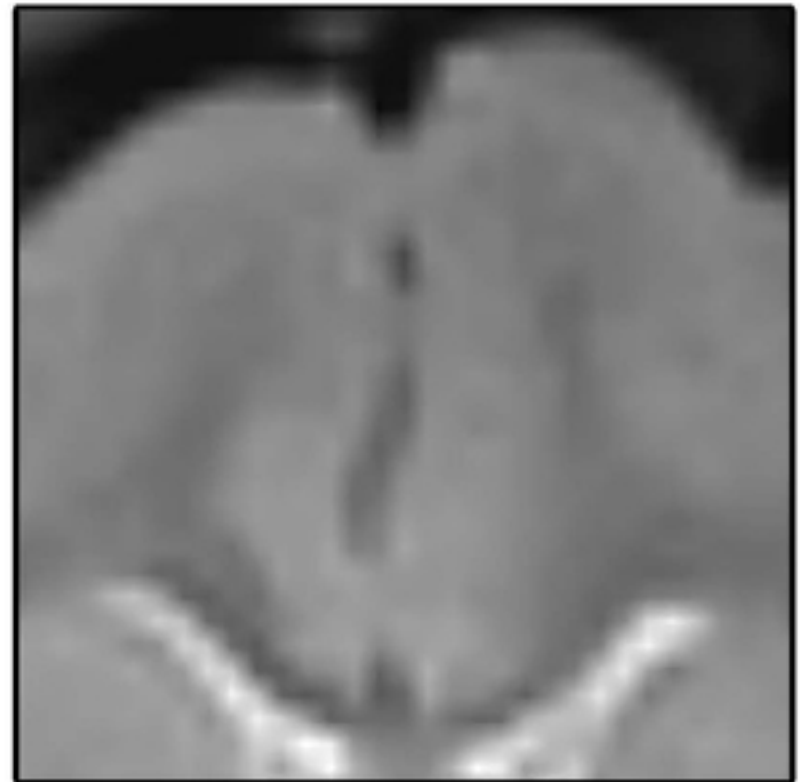
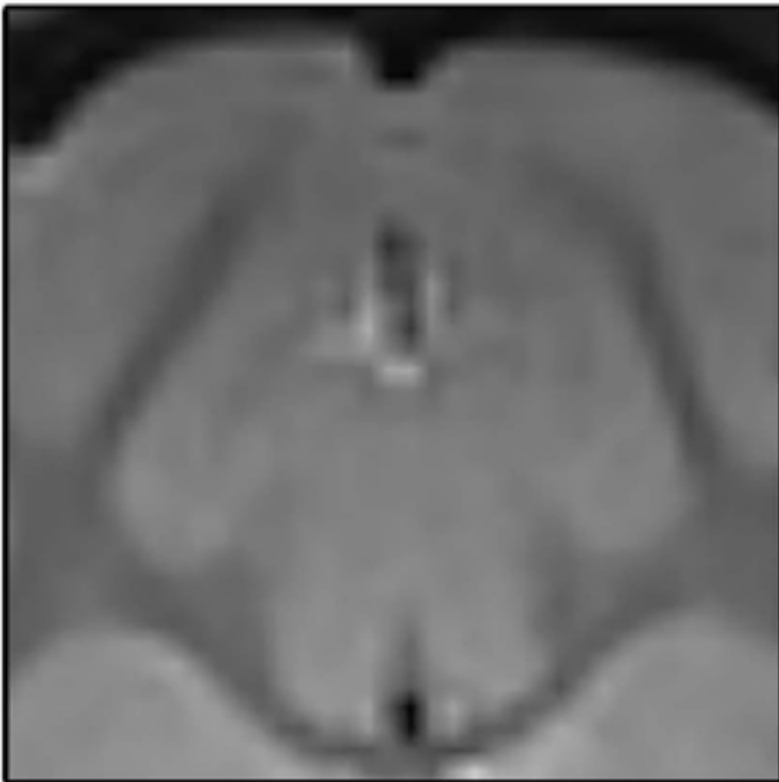
# Affected

bioRxiv preprint doi: <https://doi.org/10.1101/2020.02.14.949214>; this version posted February 14, 2020. The copyright holder for this preprint (which was not certified by peer review) is the author/funder, who has granted bioRxiv a license to display the preprint in perpetuity. It is made available under aCC-BY 4.0 International license.

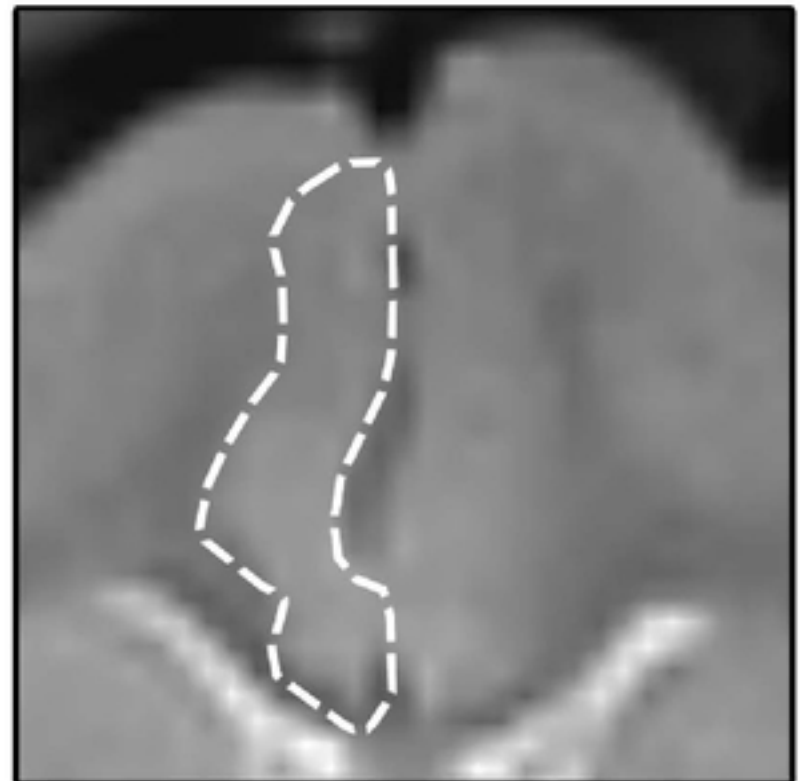
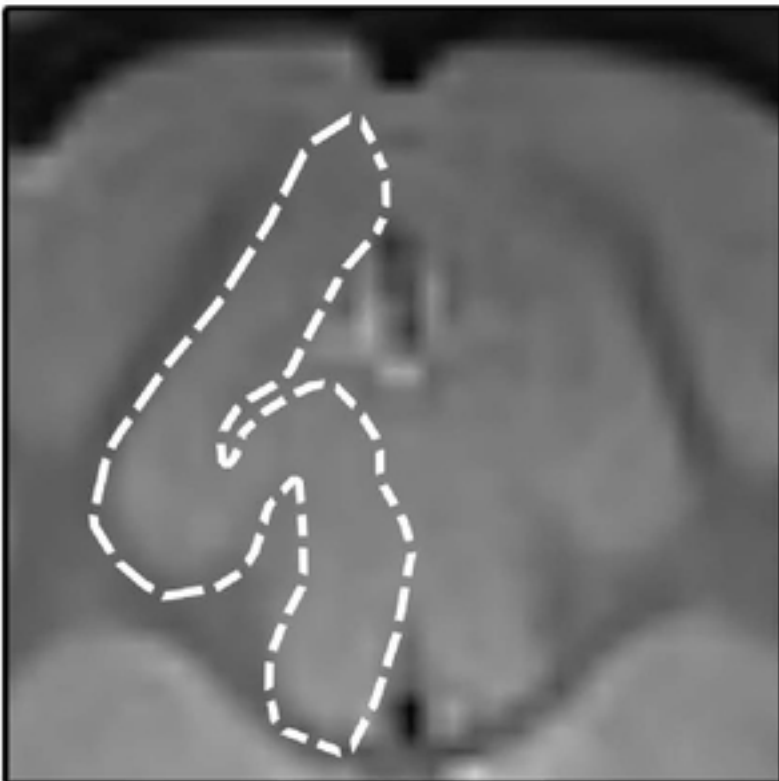
A



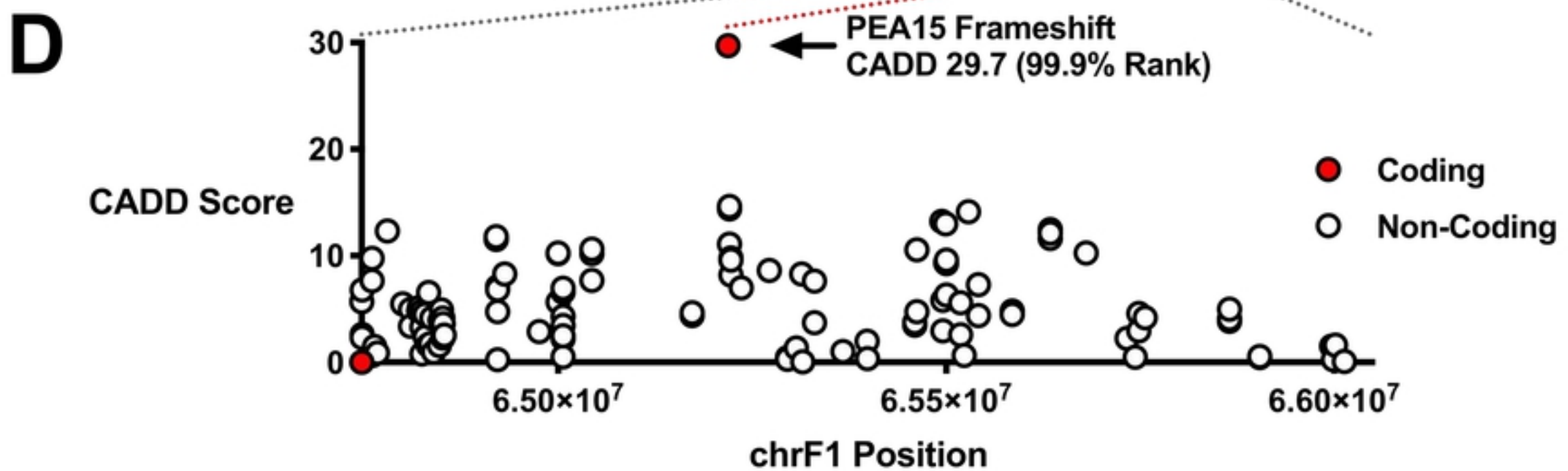
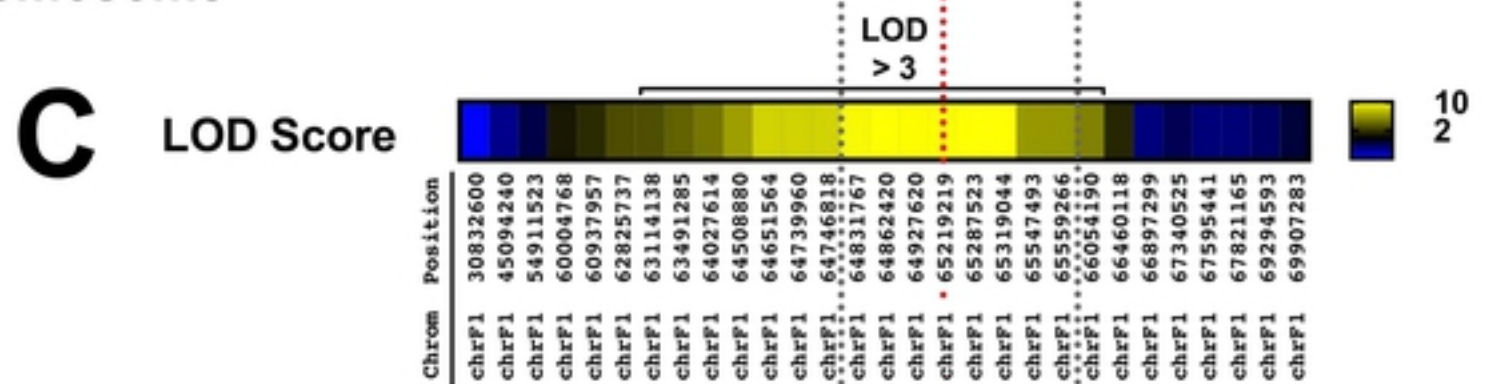
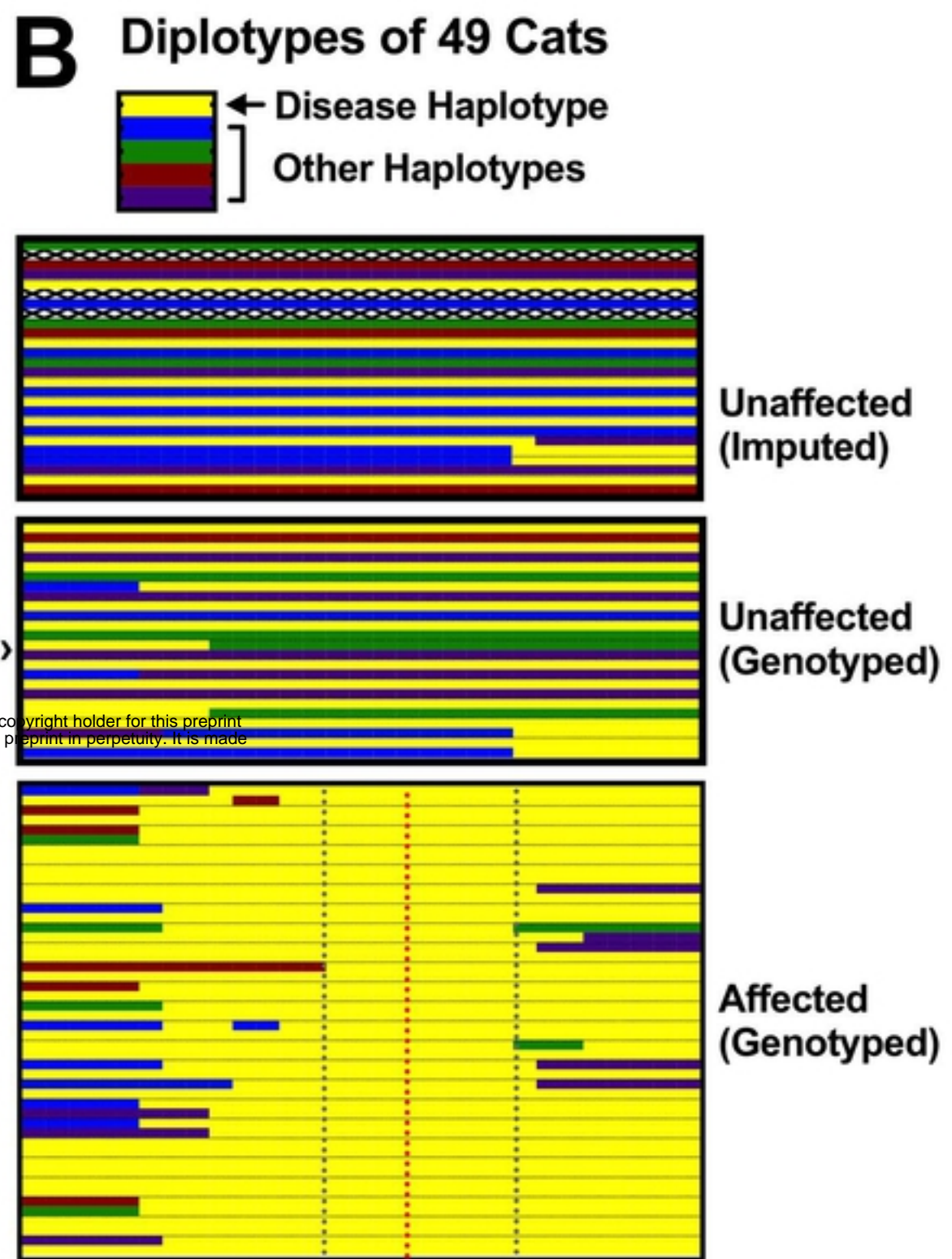
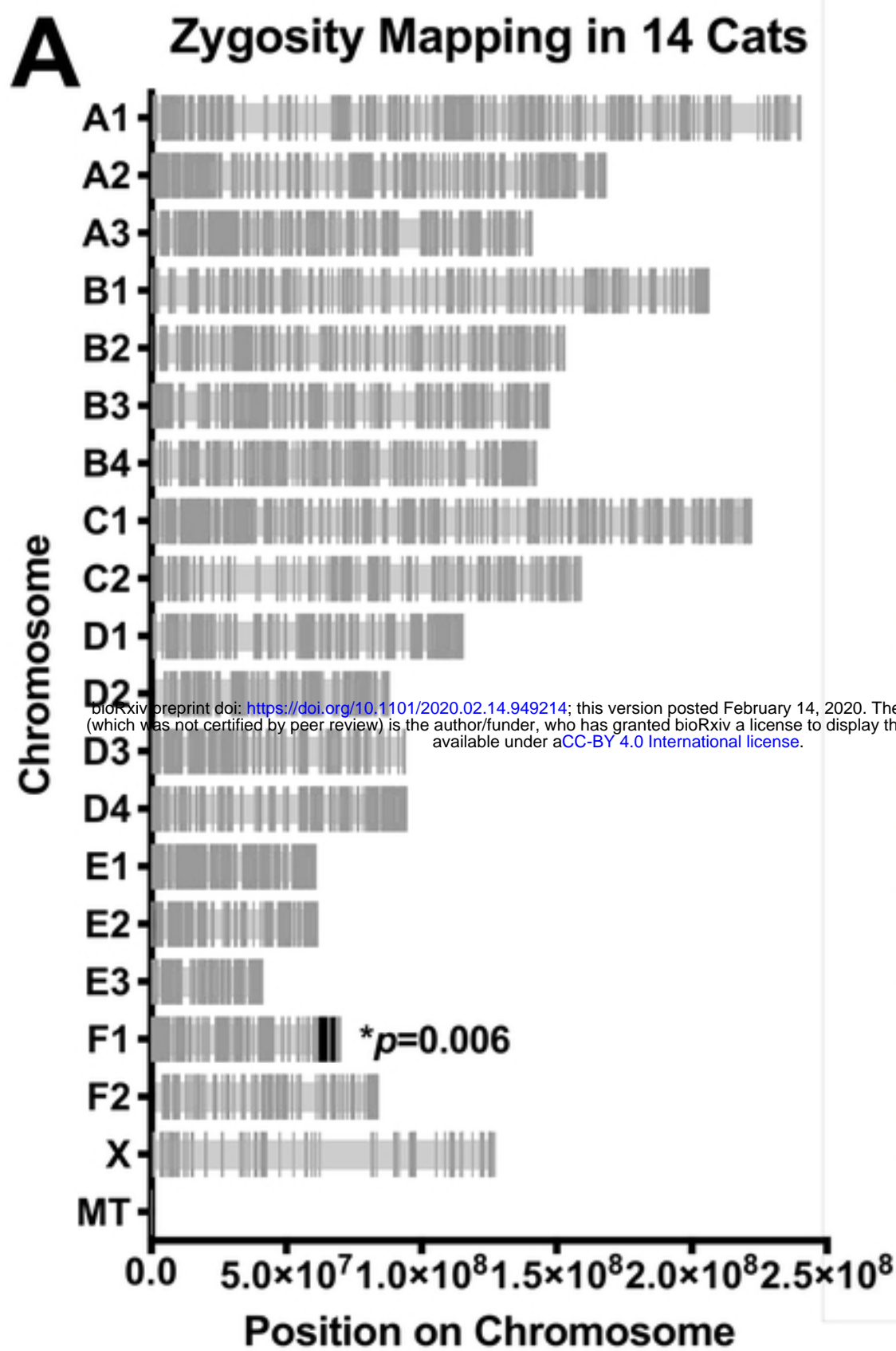
B

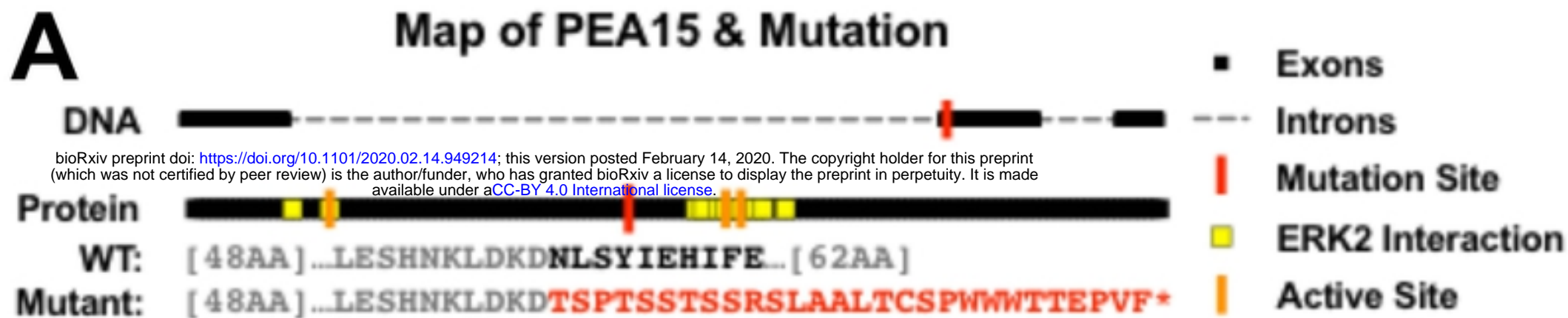


C

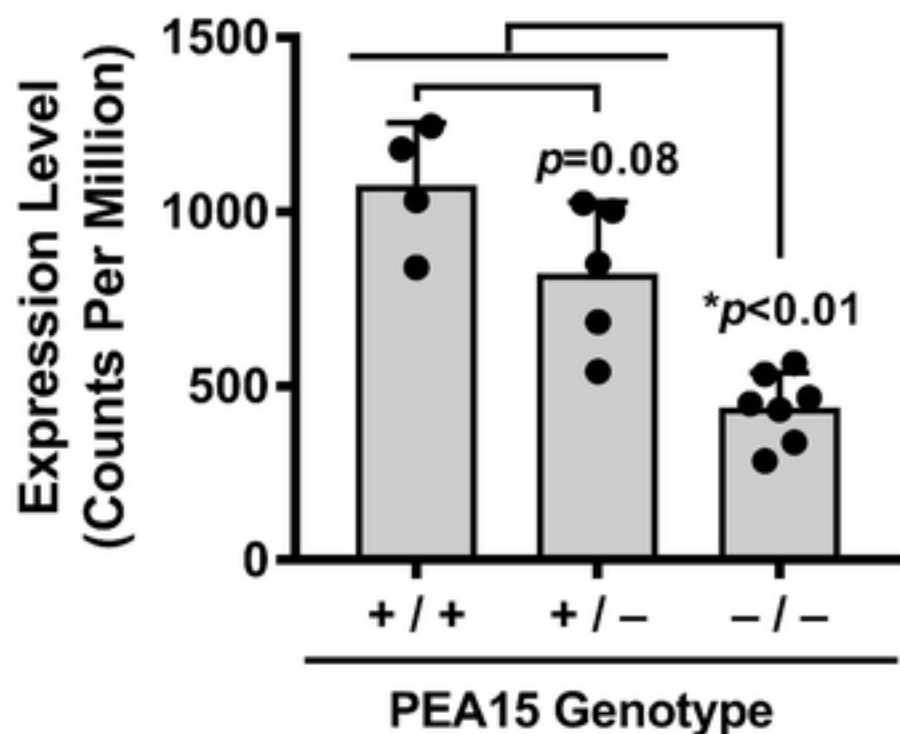




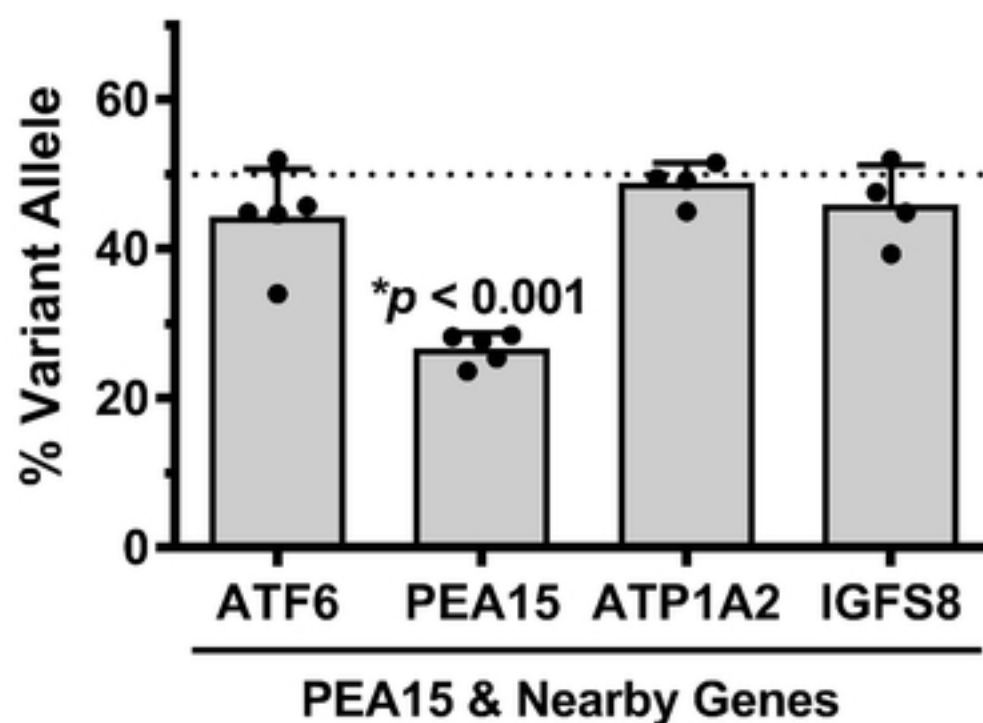




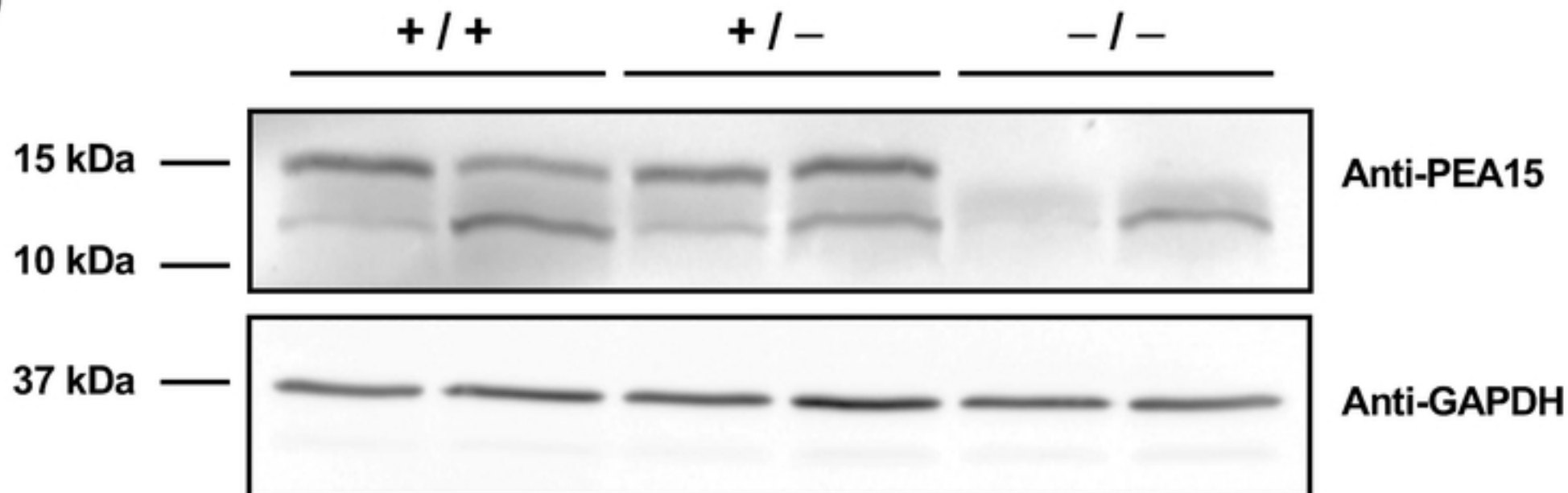
### B PEA15 Expression Level



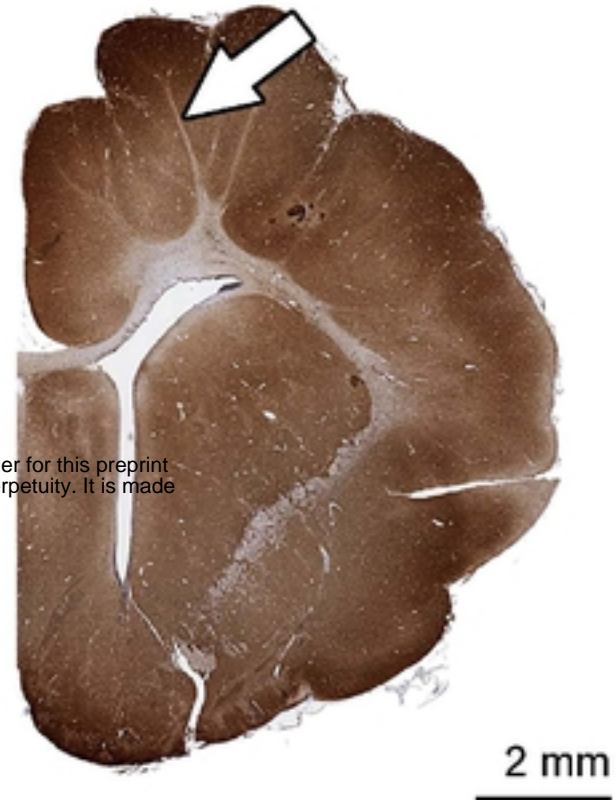
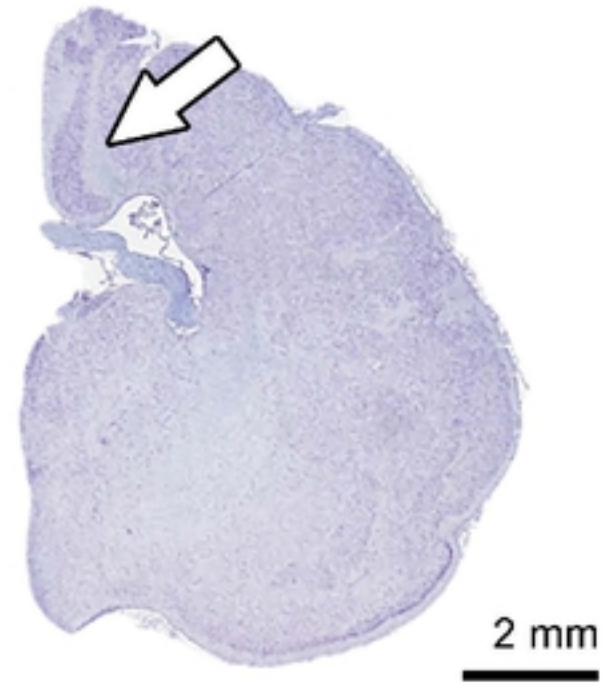
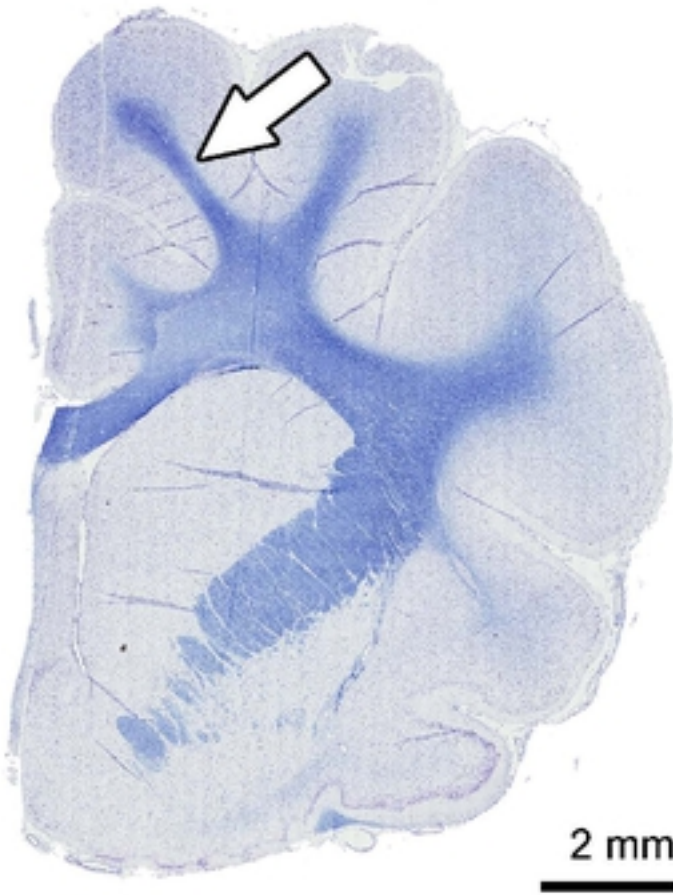
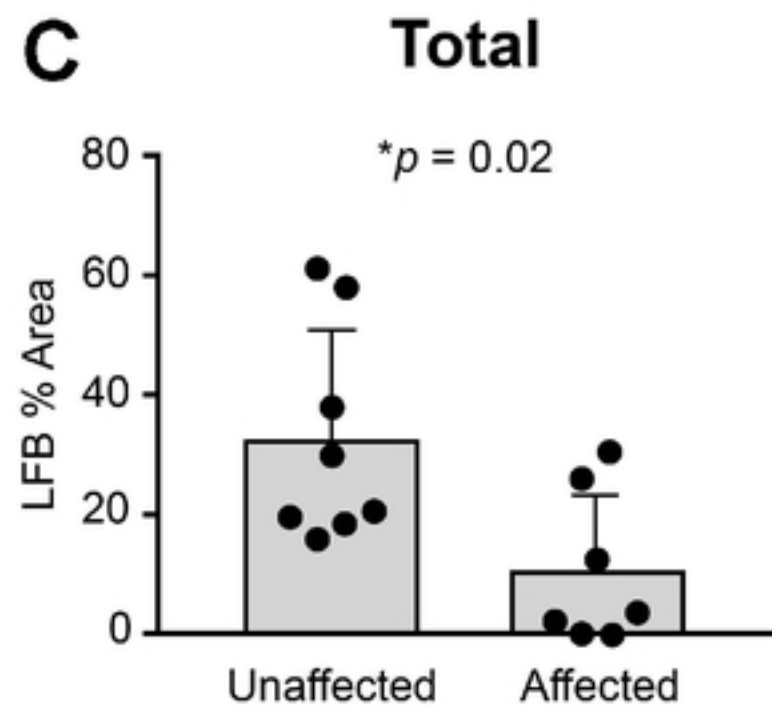
### C PEA15 Allele Bias in Heterozygous Cats



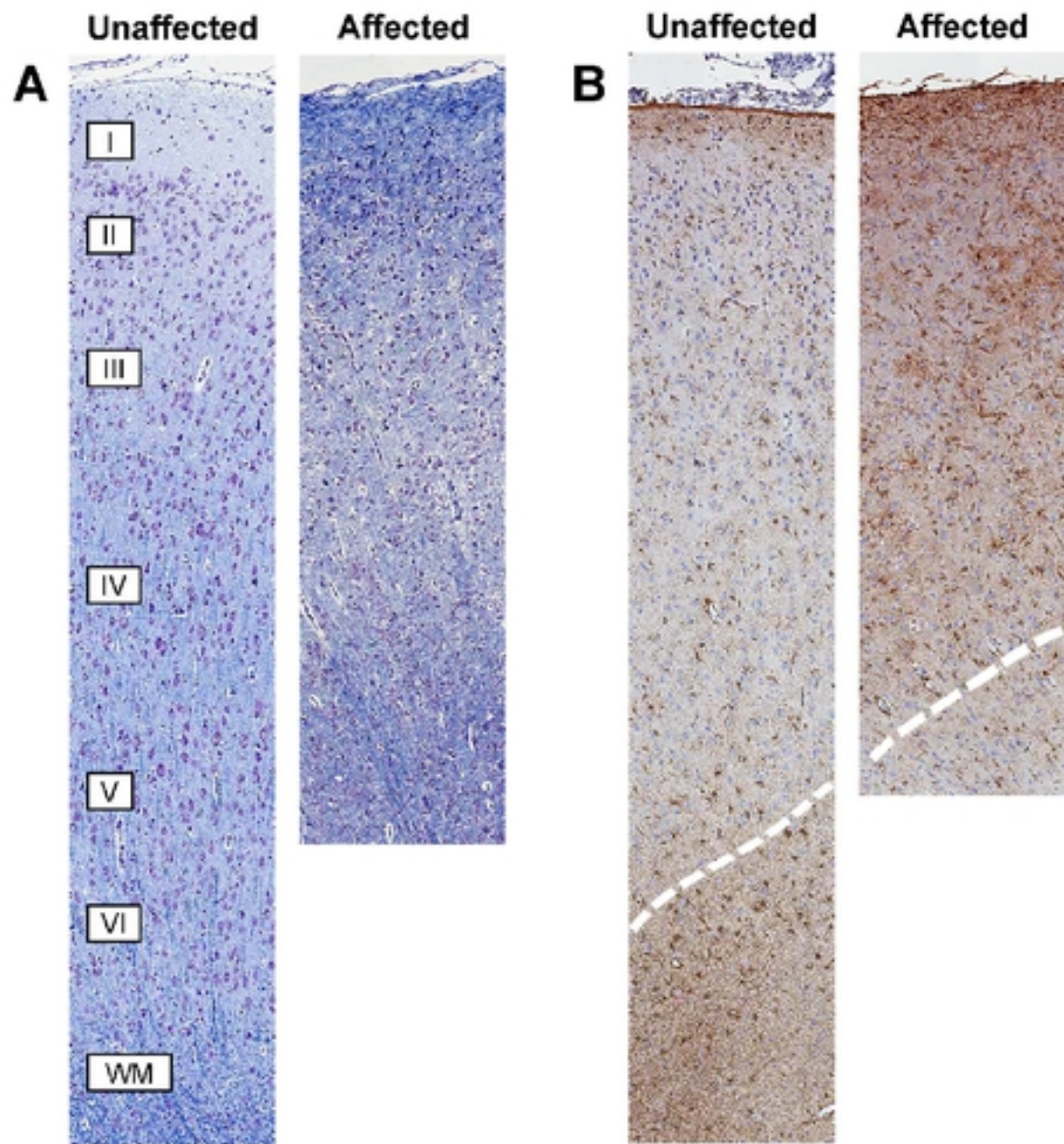
### D Western Blot for PEA15 from Cortex



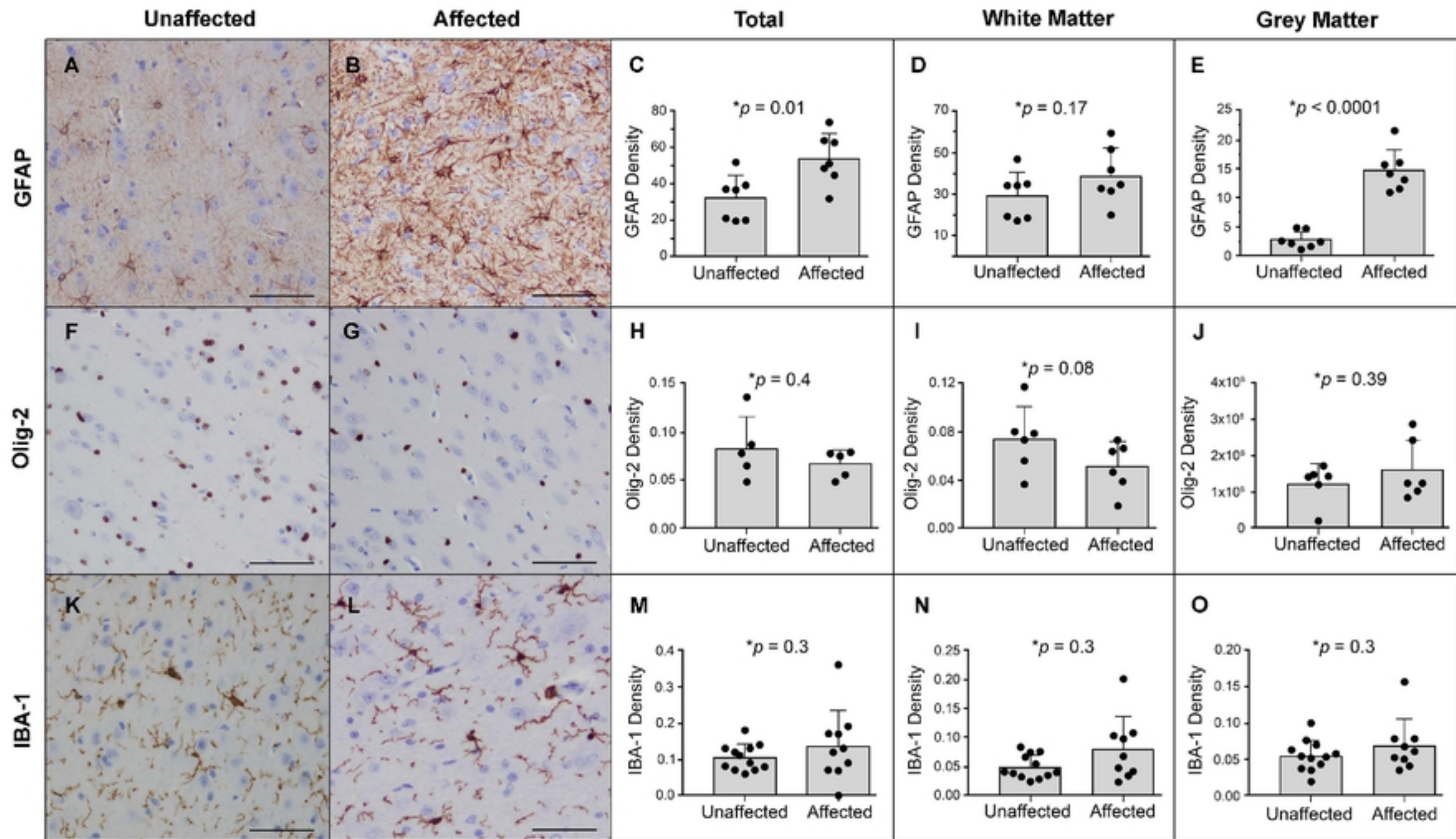


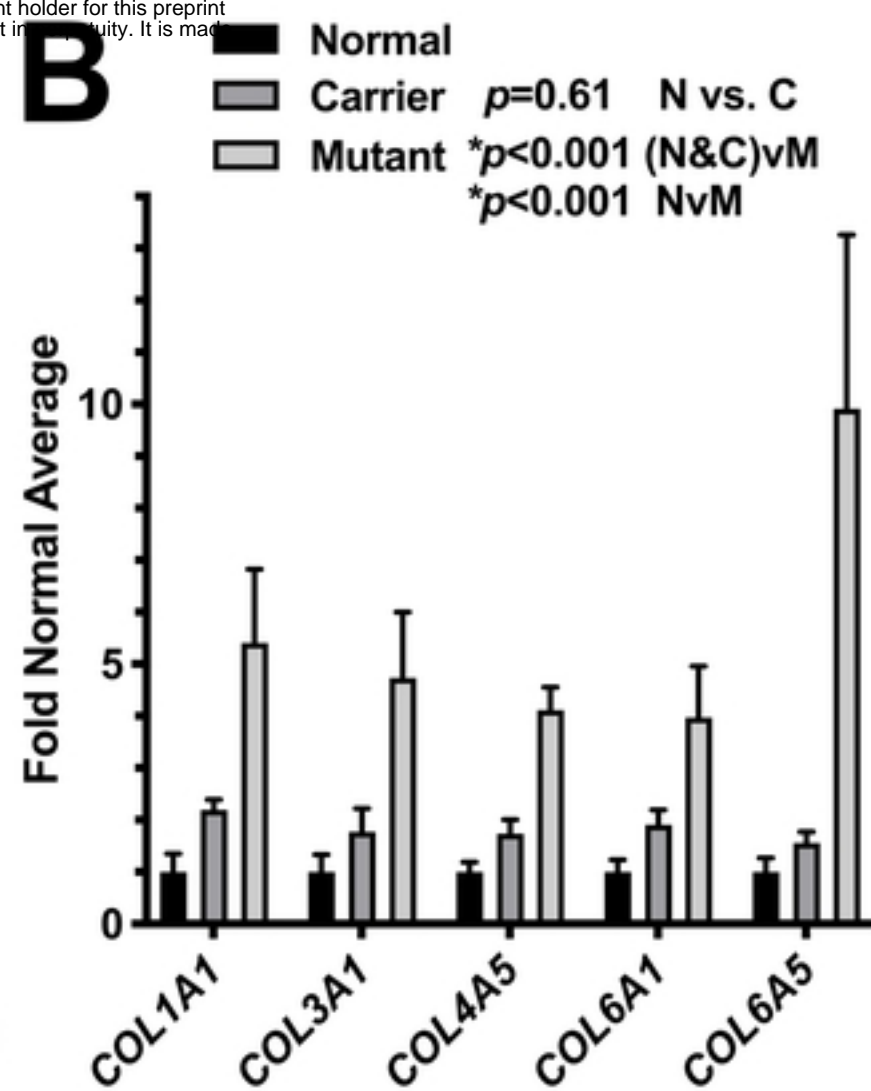
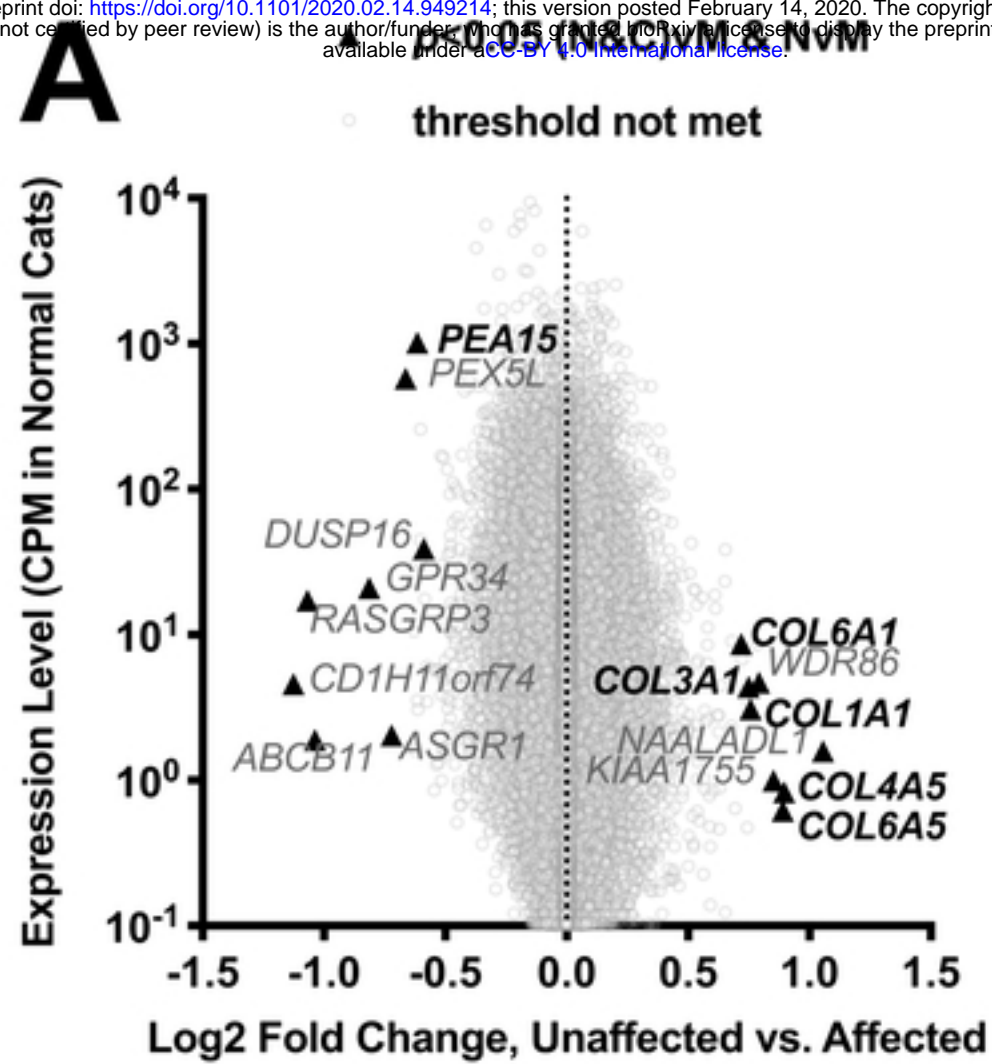
**A****B****C**



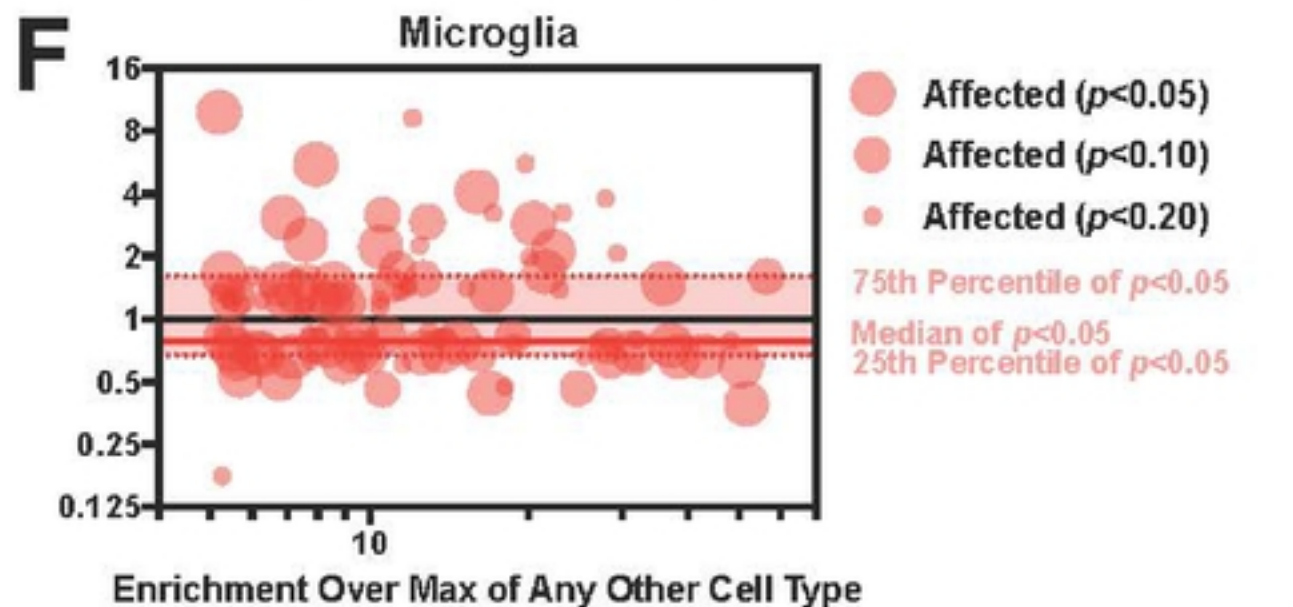
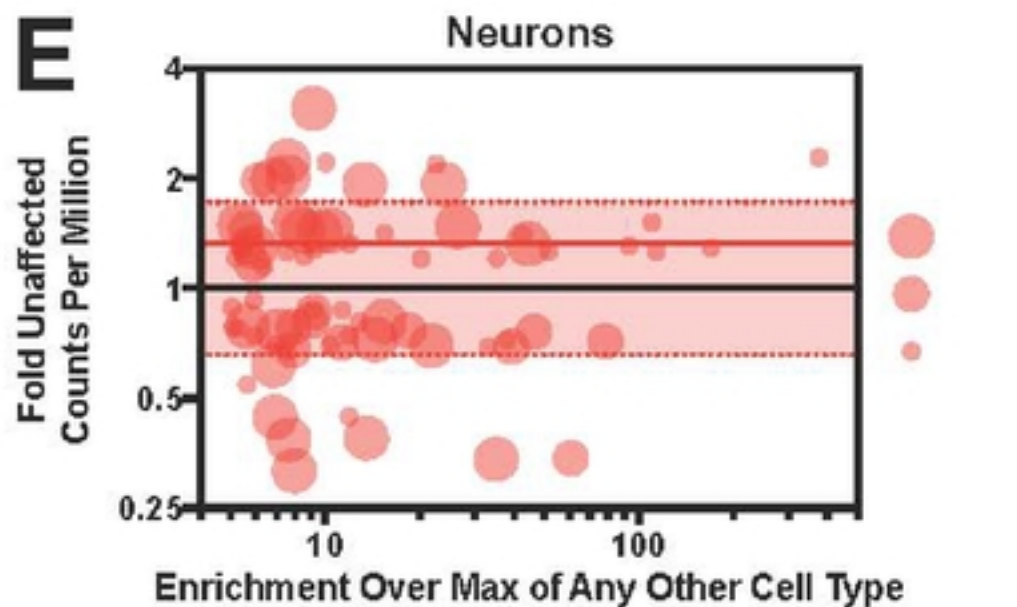
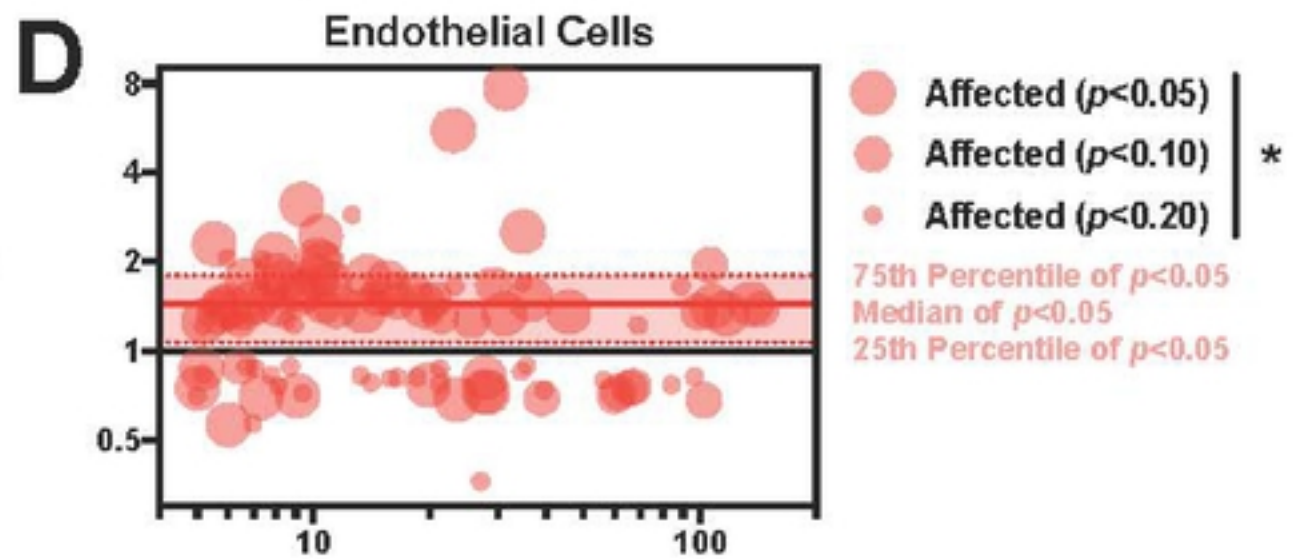
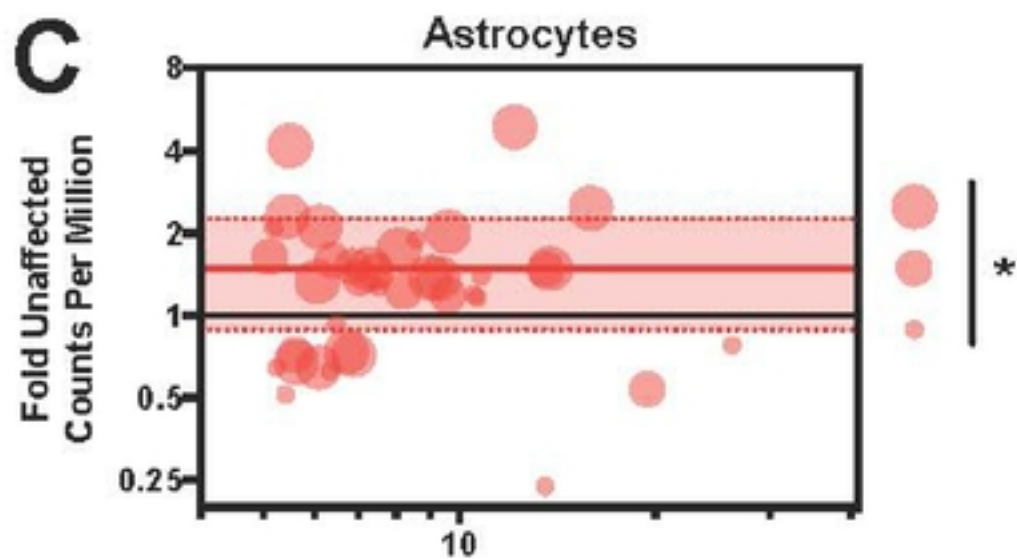
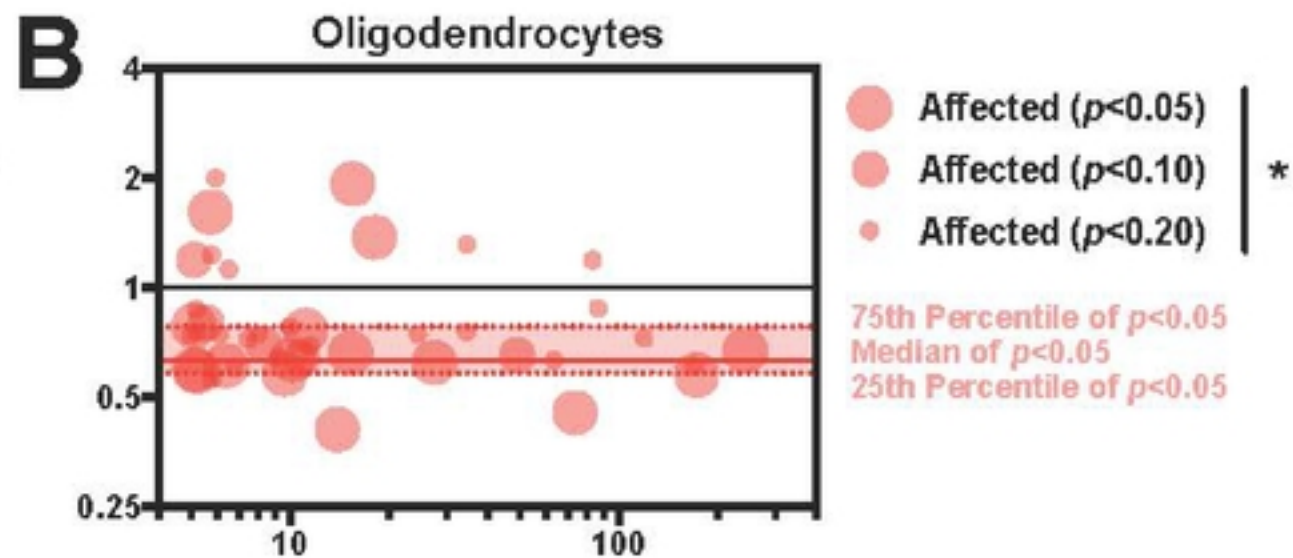
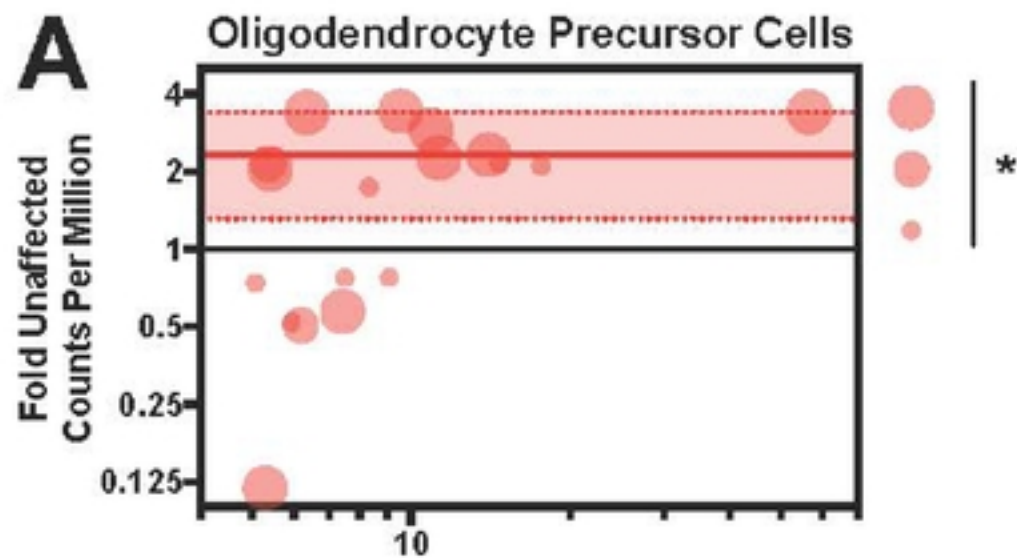




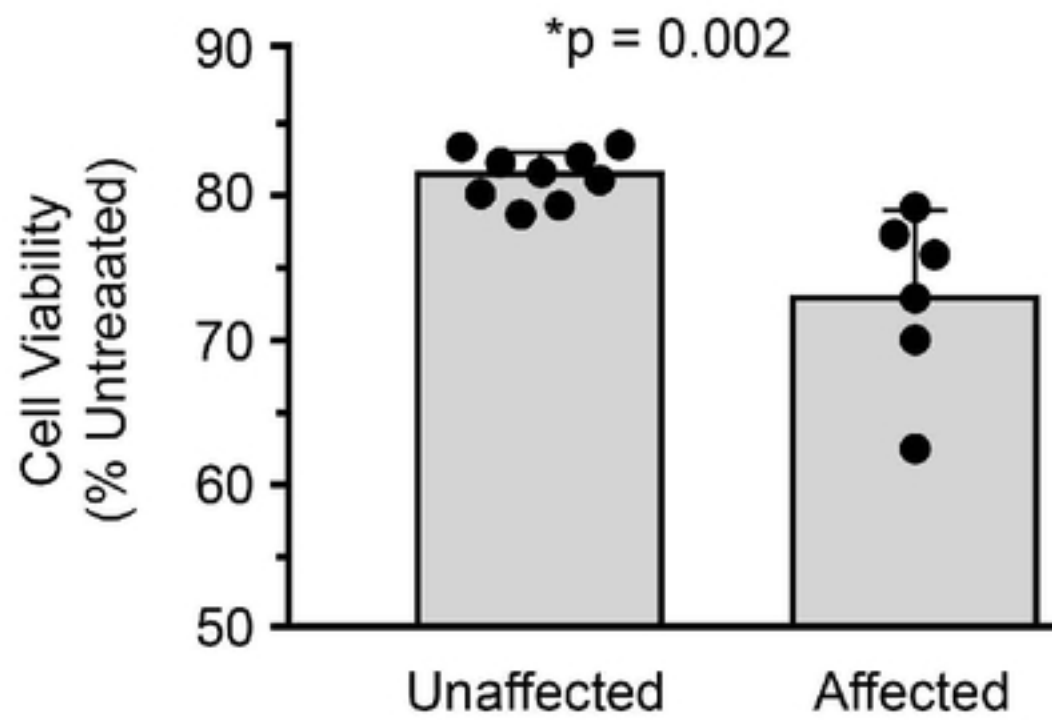






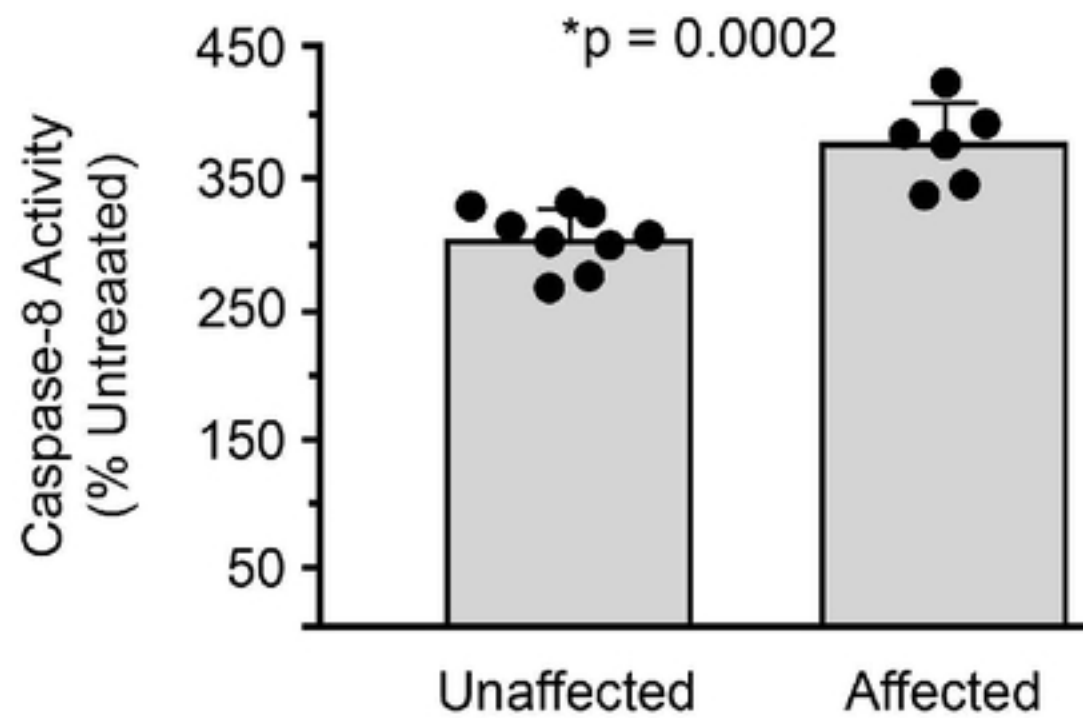


## A Cell Viability

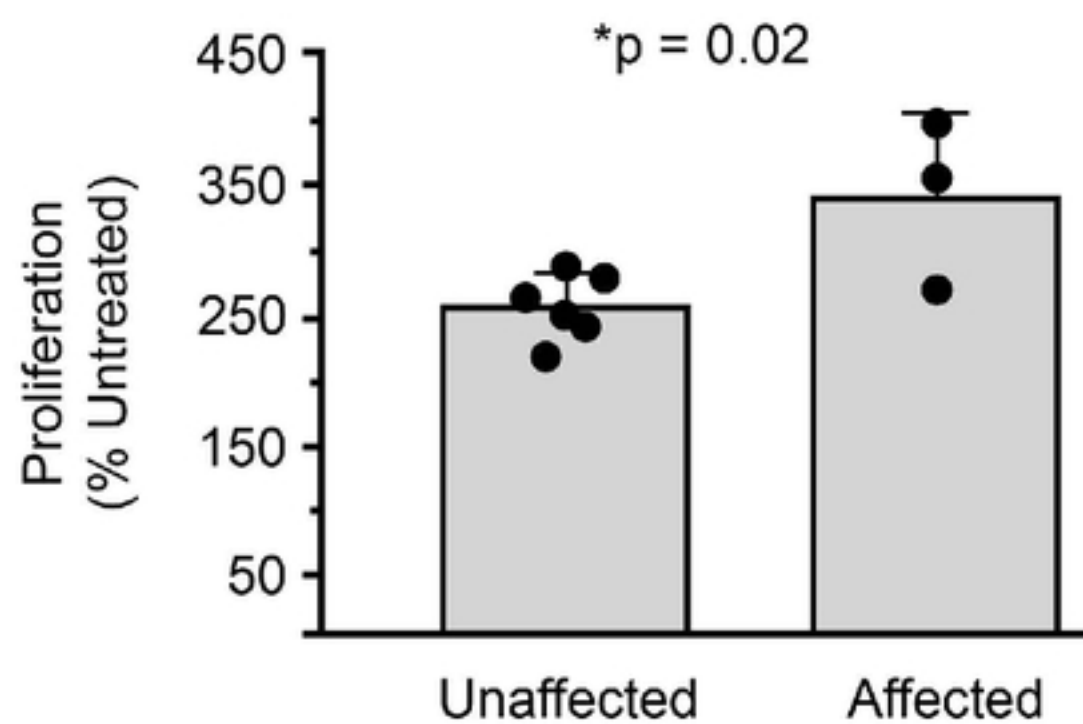


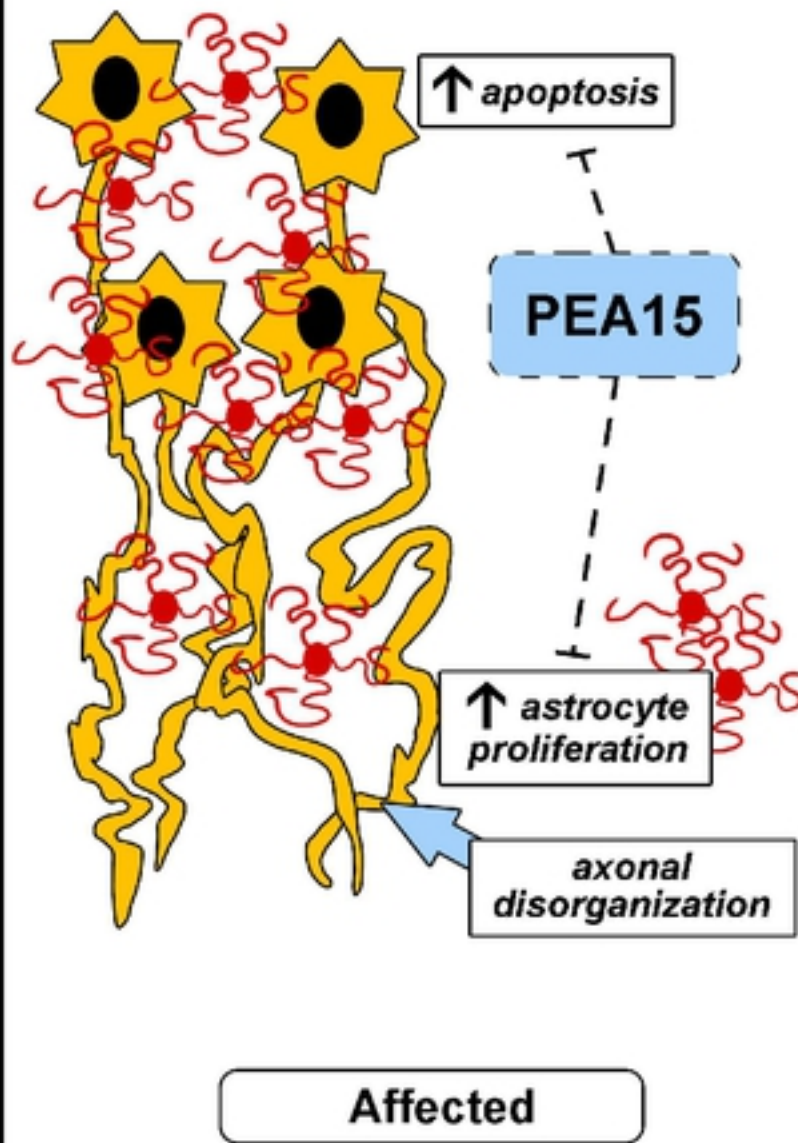
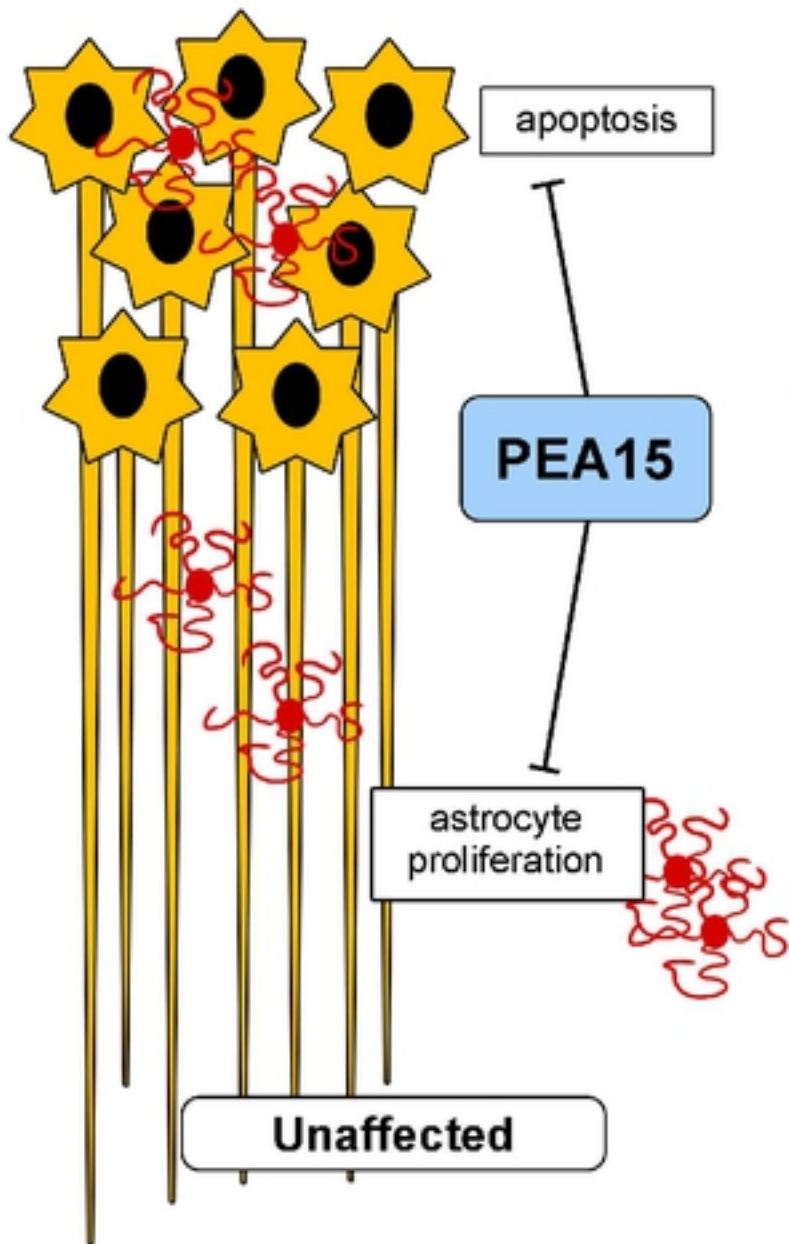
bioRxiv preprint doi: <https://doi.org/10.1101/2020.02.14.949214>; this version posted February 14, 2020. The copyright holder for this preprint (which was not certified by peer review) is the author/funder, who has granted bioRxiv a license to display the preprint in perpetuity. It is made available under aCC-BY 4.0 International license.

## B Caspase-8 Activity



## C FGFb Stimulated Proliferation





**SUMMARY**  
 During neurodevelopment, PEA15 regulates apoptosis and proliferation  
 ↓  
 Absence of PEA15 leads to increased neuronal apoptosis and astrocyte proliferation  
 ↓  
 Results in disorganized axonal development, underdeveloped white matter, microcephaly, and polymicrogyria